



Simulations of the impact of cloud condensation nuclei and ice-nucleating particles perturbations on the microphysics and radar reflectivity factor of stratiform mixed-phase clouds

Junghwa Lee¹, Patric Seifert¹, Tempei Hashino², Maximilian Maahn³, Fabian Senf¹, and Oswald Knoth¹

¹Leibniz Institute for Tropospheric Research (TROPOS), Leipzig, Germany

²School of Environmental Science and Engineering, Kochi University of Technology, Kami, Japan

³Leipzig Institute of Meteorology (LIM), Leipzig University, Leipzig, Germany

Correspondence: Junghwa Lee (lee@tropos.de)

Received: 18 August 2023 – Discussion started: 24 August 2023

Revised: 23 February 2024 – Accepted: 24 March 2024 – Published: 21 May 2024

Abstract. In this research, we delve into the influence of cloud condensation nuclei (CCN) and ice-nucleating particle (INP) concentrations on the morphology and abundance of ice particles in mixed-phase clouds, emphasizing the consequential impact of ice particle shape, number, and size on cloud dynamics and microphysics. Leveraging the synergy of the Advanced Microphysics Prediction System (AMPS) and the Kinematic Driver (KiD) model, we conducted simulations to capture cloud microphysics across diverse CCN and INP concentrations. The Passive and Active Microwave radiative TRAnsfer (PAMTRA) radar forward simulator further augmented our study, offering insights into how the concentrations of CCN and INPs affect radar reflectivities.

Our experimental framework encompassed CCN concentrations ranging from 10 to 5000 cm⁻³ and INP concentrations from 0.001 to 10 L⁻¹. Central to our findings is the observation that higher INP concentrations yield smaller ice particles, while an increase in CCN concentrations leads to a subtle growth in their dimensions. Consistent with existing literature, our results spotlight oblate-like crystals as dominant between temperatures of –20 and –16 °C. Notably, high-INP scenarios unveiled a significant prevalence of irregular polycrystals. The aspect ratio (AR) of ice particles exhibited a decline with the rise in both CCN and INP concentrations, highlighting the nuanced interrelation between CCN levels and ice particle shape, especially its ramifications on the riming mechanism.

The forward-simulated radar reflectivities, spanning from –11.83 dBZ (low INP, 0.001 L⁻¹) to 4.65 dBZ (high INP, 10 L⁻¹), elucidate the complex dynamics between CCN and INPs in determining mixed-phase cloud characteristics. Comparable differences in radar reflectivity were also reported from observational studies of stratiform mixed-phase clouds in contrasting aerosol environments. Our meticulous analysis of KiD-AMPS simulation outputs, coupled with insights into aerosol-driven microphysical changes, thus underscores the significance of this study in refining our ability to understand and interpret observations and climate projections.

1 Introduction

Clouds are still one of the most uncertain components of the global atmosphere system (Bony et al., 2015). Their formation and evolution occur on various spatio-temporal scales, which makes it virtually impossible to tackle them with single, unified observational or simulation approaches (Kahn et al., 2023). Single sub-processes are studied individually and will only in a later stage be the basis for an improved comprehensive understanding. Important components of a cloud's life cycle are, e.g., the cloud formation and the subsequent transitions from the liquid to the ice phase. The presence of the ice phase is an essential prerequisite for the production of adequate amounts of precipitation in most regions on Earth (Mülmenstädt et al., 2015). Nevertheless, for the initial formation of cloud droplets, as well as for the formation of ice crystals down to temperatures of -38°C , aerosol particles are required for the phase transition by providing a reservoir of either cloud condensation nuclei (CCN) or ice-nucleating particles (INPs), respectively (Morrison et al., 2012; Hoose and Möhler, 2012). The interplay of the abundance of CCN and INPs and the cloud evolution is an important pathway of aerosol–cloud interaction. Perturbations in the concentration and type of CCN or INPs can in particular potentially influence the formation and evolution of ice particles in mixed-phase clouds.

There are strong indications given by both observations and modeling approaches that INP and CCN perturbations do have a considerable impact on the mixed-phase cloud formation and evolution. Seifert et al. (2010) revealed increased fractions of ice-containing clouds in dust-laden cloud environments over central Europe. On a global scale, these findings were confirmed, e.g., by Zhang et al. (2018), using observations from the spaceborne A-Train satellite constellation. Hemispheric contrasts in mixed-phase clouds and their relationship to cloud turbulence and aerosol load were investigated in detail by Radenz et al. (2021), who also concluded that a measurable impact of aerosol on mixed-phase cloud formation exists. Seifert et al. (2012) revealed considerable impacts of a dust event on the simulation of clouds and precipitation patterns over Germany. Similar effects were identified in a European-scale approach by Barthlott and Hoose (2018). Fan et al. (2014) performed spectral bin simulations to investigate the influence of CCN and INPs on precipitation in two distinct mixed-phase orographic cloud scenarios characterized by different cloud temperatures. The study revealed varying degrees of significance regarding the impacts of CCN and INPs on precipitation, with the INPs exhibiting a more pronounced effect in both cases. Furthermore, Fan et al. (2017) conducted a sensitivity analysis where they systematically varied the concentrations of CCN and INP proxies across a wide range, spanning from extremely low to extremely high concentrations, employing spectral bin modeling specifically tailored to orographic mixed-phase clouds.

Also on a global scale, aerosol variations were found to be key for understanding the variability of mixed-phase clouds (Atkinson et al., 2013). Recently, even the first closure studies bridging remote sensing observations of CCN and INPs with those of cloud droplet concentration and ice crystal number concentration were initiated (Ansmann et al., 2019; Engelmann et al., 2021). However, simulations and observational approaches have to date rarely been combined, which hinders one from drawing specific conclusions on aerosol effects on mixed-phase clouds. One key approach is to connect cloud-resolving, aerosol-sensitive ideally spectral bin models with forward operators in order to transfer simulation output into observation space. By doing so, simulations for selected scenarios can be evaluated against real-world observations.

Given the complexity of spectral bin modeling frameworks, it is essential to incorporate the most relevant processes on the one hand and to constrain the environmental conditions to a maximum but still realistic state on the other hand. Besides number concentration, particle habit should thus also be incorporated into respective aerosol–cloud interaction studies which aim at a closure against observations. Ice particle shape plays a crucial role in determining the microphysical and radiative properties of mixed-phase and ice clouds (Mishchenko et al., 1996; McFarquhar and Heymsfield, 1997). The diverse shapes of ice particles influence their growth, aggregation, and riming processes, which in turn affect cloud lifetime, precipitation formation, and radiative energy transfer within the atmosphere (Magono and Lee, 1966; Heymsfield and Westbrook, 2010; Um and McFarquhar, 2011). The complexity and diversity of ice particle shapes present challenges for both cloud microphysics modeling and remote sensing of cloud properties. A comprehensive understanding of ice particle shape is essential for improving the accuracy of cloud microphysics models, remote sensing retrievals, and ultimately climate predictions (Liou and Ou, 2004; Tao et al., 2012; Chen and Liu, 2016; Vázquez-Martín et al., 2021). Despite its importance, the representation of ice particle shape in cloud microphysics models remains a significant challenge. Many models adopt simplified assumptions regarding ice particle shape, such as assuming all particles are spherical or using a limited set of predefined shapes (Mitchell, 1996; Morrison et al., 2005; Cotton et al., 2013). These simplifications can introduce uncertainties and biases in the simulated cloud properties and their interactions with radiation (Cotton et al., 2013). Furthermore, the complex nature of ice particle shape and its dependence on factors such as temperature, supersaturation, and aerosol loading add to the difficulty in accurately representing this aspect of cloud microphysics (Bailey and Hallett, 2009; Kanji et al., 2017).

Radar remote sensing is a valuable tool for observing ice particles in clouds, providing insights into their size, shape, and spatial distribution (Hogan et al., 2000; Westbrook and Illingworth, 2011). However, interpreting radar observations of ice particles requires a thorough understanding of the re-

relationship between ice particle shape and the radar variables, such as reflectivity and Doppler velocity (Hogan et al., 2012; Kneifel et al., 2015). Radar forward simulators, which generate synthetic radar observations based on cloud model outputs, can help bridge this gap by allowing researchers to systematically investigate the sensitivity of radar variables to different ice particle shapes and model assumptions (Matsui et al., 2019).

In this study, we utilize the Advanced Microphysics Prediction System (AMPS) coupled with the Kinematic Driver (KiD) to conduct idealized simulations of mixed-phase cloud microphysics (Hashino and Tripoli, 2007, 2008, 2011a, b), incorporating a comprehensive representation of ice particle shapes and the effects of CCN and INP perturbations. AMPS is a state-of-the-art cloud microphysics model that has been specifically designed to capture the complex interactions between aerosols, cloud droplets, and ice particles with a habit prediction system (Hashino and Tripoli, 2007, 2008, 2011a). The AMPS model coupled with large-eddy simulations (LESs) successfully reproduces features of mixed-phase clouds and has been compared to observations (Hashino et al., 2020; Ong et al., 2022). To investigate the impact of ice particle shape on radar retrievals, we employ the Passive and Active Microwave radiative TRANSfer (PAMTRA) radar forward simulator. PAMTRA is a versatile tool that can simulate passive and active microwave observations of the atmosphere, accounting for the scattering properties of various ice particle shapes (Mech et al., 2020). By combining the capabilities of AMPS and PAMTRA, this study aims to provide a comprehensive understanding of the role of ice particle number size distribution and shape in mixed-phase cloud microphysics and remote sensing retrievals under varying CCN and INP conditions. Furthermore, we seek to evaluate the impact of ice particle shape assumptions and CCN and INP perturbations on the accuracy and reliability of cloud property retrievals from radar observations.

This paper is organized as follows. Section 2 briefly describes the Kinematic Driver (KiD) (Shipway and Hill, 2012) as the dynamical model and AMPS as the microphysics model. Section 3 gives information on the initial thermodynamic condition and experimental design for simulations. Section 4 shows the numerical simulation results for steady-state mixed-phase cloud cases under varying CCN and INP scenarios. Finally, Sect. 5 concludes the paper with a summary of the results.

2 Model description and simulation setup

2.1 KiD (dynamic model)

The KiD model provides a framework for examining cloud microphysics, enabling us to assess and compare different parameterizations, which leads to a better understanding of cloud particle interactions and the influence of aerosols on cloud development. The model's versatility allows its appli-

cation in the study of various cloud types, including stratiform mixed-phase and convective clouds. It has significantly contributed to the enhancement of cloud microphysical parameterizations in larger-scale models (Klein et al., 2009; Shipway and Hill, 2012).

The model accommodates a variety of microphysics schemes, from the simpler one-moment bulk models (Thompson et al., 2004) to more complex two-moment schemes (Thompson et al., 2008; Morrison et al., 2009; Shipway and Hill, 2012; Hill et al., 2015; Vié et al., 2016; Miltenberger et al., 2018). It is also compatible with detailed spectral bin microphysics schemes, including the Tel Aviv University bin microphysics and the AMPS (Tzivion et al., 1987, 1989; Hashino and Tripoli, 2007, 2008, 2011a, b; Lebo and Seinfeld, 2011; Onishi and Takahashi, 2012), as well as with Lagrangian cloud models (LCMs) (Andrejczuk et al., 2010; Arabas et al., 2015; Hoffmann et al., 2015; Dziekan et al., 2019). Further details on these aspects are provided in Shipway and Hill (2012) and Hill et al. (2023).

We emphasize the KiD framework's effectiveness in efficiently evaluating the performance of different microphysics schemes. Additionally, the KiD model functions as a valuable benchmarking tool, enabling researchers to evaluate and enhance cloud microphysics parameterizations. By comparing the results of various parameterizations within the KiD framework, inconsistencies and areas for improvement can be identified and investigated.

2.2 AMPS (microphysics model)

In this study, we employed the Kinematic Driver (KiD) model in conjunction with the Advanced Microphysics Prediction System (AMPS) to simulate mixed-phase clouds. The AMPS model has been coupled with other dynamic models such as the University of Wisconsin Nonhydrostatic Modeling system (Hashino and Tripoli, 2007, 2008; Hashino et al., 2020) and the Scalable Computing for Advanced Library and Environment (SCALE) large-eddy simulation model (Ong et al., 2022), demonstrating its capability to accurately predict mixed-phase clouds and exhibiting favorable comparisons with observational data.

According to Hashino and Tripoli (Hashino and Tripoli, 2007, 2008, 2011a, b), the AMPS microphysical model employs the Spectral Ice Habit Prediction System (SHIPS), which incorporates particle property variables (PPVs) to characterize the physical structure of ice particles, as detailed in Table 1. The SHIPS continuously updates the PPVs for each mass bin in response to evolving ambient conditions, ensuring accurate particle property diagnoses based on the PPVs.

The identification of ice particle type and habit relies on various components, including mass content, length, and concentration. In our methodology, the SHIPS defines the ice particle model as a conceptual shape to represent ice particles leading to their genesis, encompassing “pristine crys-

Table 1. List of the 16 particle property variables (PPVs) within liquid and ice spectra across each bin, as utilized in the KiD-AMPS model. Here, ρ_m denotes the moist air density, while ρ_{lat} and ρ_{iat} specify the total aerosol density within the liquid phase and ice phase, respectively. Additionally, ρ_{las} and ρ_{ias} correspond to the soluble aerosol density in the liquid and ice phases.

Spectrum	PPV	Description
Liquid	ρ_{lat}/ρ_m	Mixing ratio of total aerosol mass
	ρ_{las}/ρ_m	Mixing ratio of soluble aerosol mass
Ice	ρ_{cry}/ρ_m	Mixing ratio of crystal mass
	ρ_{rim}/ρ_m	Mixing ratio of riming mass
	ρ_{agg}/ρ_m	Mixing ratio of aggregate mass
	ρ_{frz}/ρ_m	Mixing ratio of frozen mass
	ρ_{mlt}/ρ_m	Mixing ratio of meltwater mass
	ρ_{iat}/ρ_m	Mixing ratio of total aerosol mass
	ρ_{ias}/ρ_m	Mixing ratio of soluble aerosol mass
	n_{exice}	Extra crystalline structure number
	V_{cs}	Circumscribing volume
	l_a^3	Cube of the a -axis length
	l_c^3	Cube of the c -axis length
	l_d^3	Cube of the d -axis length (cube of the dendritic arm)
	a_g	Center of gravity along the a axis
	c_g	Center of gravity along the c axis

tals, aggregates, rimed aggregates, graupel, and rimed crystals” as explicated in Fig. 2 by Hashino and Tripoli (2007). Pristine crystals, rimed crystals, aggregates, and rimed aggregates are modeled as cylinders, while graupel is represented as a spheroid. These shapes serve as the basis for determining the maximum dimension (D) of each particle. However, it is important to note that this diagnosis is primarily intended for comparison with observations or other models using predicted mass bin information within the PPVs. Therefore, additional errors may arise when artificially categorizing these types. In this study, we analyzed the mass bin information without separate type divisions for a more comprehensive assessment.

The habit of ice crystals, a critical aspect of our study, is determined by analyzing their unique crystallographic properties, which include forms such as plates, dendrites, columns, and three polycrystals, as illustrated in Fig. 1. For each identified particle habit, the SHIPS within the AMPS model assigns an ice particle model that represents the geometric shape enveloping the ice particle. This model encompasses detailed crystal habit information – such as the a -axis length (l_a), representing the radius; the c -axis length (l_c), representing the height; and the d -axis length (l_d), representing the dendritic arm – across the three crystal habits of plate, columnar, and dendrite for monocrystals. Additionally, the model employs a PPV, termed the extra crystalline structure number (n_{exice}), which ranges from 0 to 1. A value of n_{exice} greater than or equal to 0.5 signifies that the ice crystals in a particular bin are polycrystals. The SHIPS’s methodical approach also integrates the coordinates of the center of gravity (a_g , c_g), measured along the a and c axes from the center of the monocrystals, as distinct PPVs. These measurements are

pivotal in differentiating between planar and columnar polycrystals: a planar polycrystal is identified if the ratio a_g/l_a exceeds the ratio c_g/l_c by more than 0.5, whereas a columnar polycrystal is determined if c_g/l_c exceeds a_g/l_a by more than 0.5. Ice crystals that do not fit within these criteria, such as scale-like side planes, are categorized as irregular polycrystals. The process and criteria for habit diagnosis are further detailed in Fig. 2.

To explain more about ice particle habit, the ice crystal growth regime is determined based on the cumulative relative frequency of habits and a random number generator when the temperature falls below -20°C and the maximum dimension of the crystal is less than $20\ \mu\text{m}$. The growth regime is initially selected from polycrystalline, columnar, and planar hexagonal regimes. If the growth regime is polycrystalline, a random number determines whether it is columnar or planar polycrystalline. Furthermore, if it is polycrystalline, another random number determines the growth regime for a hexagonal monocrystal. This implies that small ice crystals can grow differently from the habit diagnosed at the beginning of the time step. Conversely, for temperatures above -20°C , it is assumed that polycrystals do not form. Once the maximum dimension exceeds $20\ \mu\text{m}$, the ice crystal is presumed to follow the growth of the diagnosed habit at the beginning of the time step.

Expanding upon this, the concept of AR of an object is the ratio of its width to its height. In this study, the AR of polycrystalline ice particles is determined by the ratio of the semi-axis lengths of the ice particle model, i.e., $\alpha = l_{c,\text{sm}}/l_{a,\text{sm}}$, while the AR of monocrystalline particles is determined by the ratio of the axis lengths, $\alpha = l_c/l_a$.

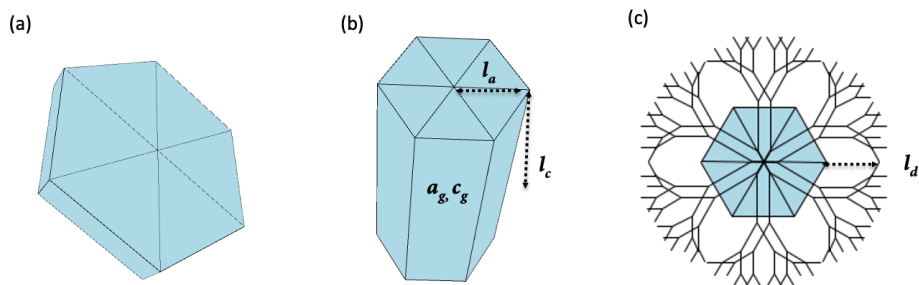


Figure 1. Diagnosis of the habit of the representative hydrometeor dimensions (l_a , l_c , and l_d) for monocrystals, including (a) hexagonal plate, (b) column, and (c) dendrite.

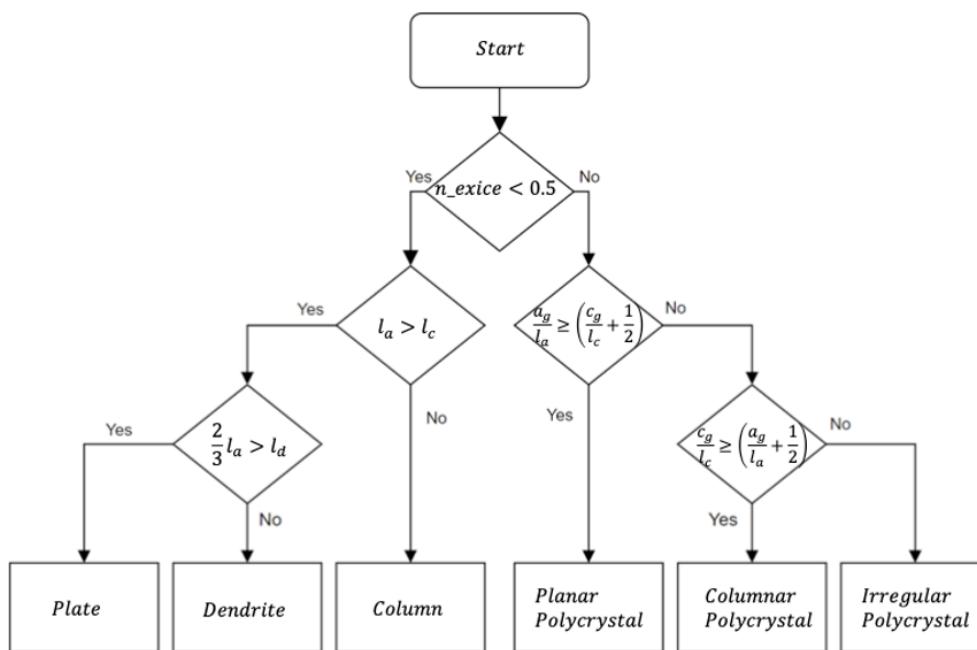


Figure 2. Flowchart depicting the diagnostic procedure for identifying ice particle habits in the AMPS.

Within the framework of the AMPS model, ice particles are characterized by their circumscribing sphere volume, denoted as V_{cs} . This volume is pivotal for comprehending the microphysical behavior of ice particles within mixed-phase clouds. As Hashino and Tripoli (2011a) explain, the circumscribing sphere volume of an ice particle is instrumental in forecasting the mass–dimension (m–D) relationship. The AMPS model utilizes functions that interlink the predicted sphere volume with the diagnosed aspect ratios, semi-axis lengths, and the particle’s maximal extent. Each mass bin’s circumscribing sphere volume, a key PPV, is integral to these prognostications. The model assumes a consistent geometric form across microphysical processes, transferring the concentration-weighted circumscribing sphere volume between mass bins as per the collection process. This transfer is essential to ascertain the circumscribing sphere volume of representative hydrometeors, thereby ensuring an accurate representation of the ice particles’ physical properties. More-

over, this factor critically influences the determination of the effective diameter. The formulation for calculating V_{cs} depends on the particle type: for most ice particles, it is determined by the equation $k_s(l_{a,sm})^3(1+\alpha^2)^{3/2}$ assuming a cylinder, where $k_s = 4\pi/3$, and α represents the aspect ratio (AR) of the ice particle defined as the ratio of the vertical semi-axis length ($l_{c,sm}$) to the horizontal semi-axis length ($l_{a,sm}$). However, for graupel, it is computed using $k_s(l_{a,sm})^3 \max(1, \alpha^3)$ assuming an ellipsoid.

It is important to highlight that while categorizing solid hydrometeors into specific types and habits is not obligatory for conducting SHIPS microphysics simulations, it greatly improves the model verification process. This is especially valuable because observational data are frequently organized based on these conventional classifications, facilitating more robust model comparisons. Given this capability, we conclude that AMPS is well suited to investigate the impact of varying CCN and INP conditions on particle shape.

2.3 PAMTRA (radar forward simulator)

The equivalent radar reflectivity factor denoted as Z_e , characterizes the collective scattering properties of a volume of scatterers, such as atmospheric precipitation particles, rather than just a single object. This factor is crucial in identifying and quantifying precipitation events by enabling the detection of radar signal reflections from these particles. The magnitude of Z_e is influenced by several factors: the size and concentration of the precipitation particles, their composition, and the frequency of the radar signal.

To convert the model data into radar variables, we utilize PAMTRA, a powerful tool designed for simulating and retrieving microwave radiative properties in the atmosphere. Serving as a forward model, PAMTRA allows the interpretation of data from diverse passive and active microwave sensors, including radars and radiometers, used for observing and studying precipitation and other atmospheric phenomena. PAMTRA incorporates crucial factors such as cloud and precipitation scattering as well as gas absorption and facilitates comprehensive analysis of remote sensing data from satellite, airborne, and ground-based platforms. Numerous studies have leveraged PAMTRA to investigate precipitation processes, cloud microphysics, and remote sensing of atmospheric variables, establishing it as an invaluable resource for researchers and atmospheric scientists engaged in the field of radiative transfer and remote sensing (Maahn et al., 2019; Ori et al., 2020; Schnitt et al., 2020; von Lerber et al., 2022).

PAMTRA offers a full-bin interface with several benefits, which can directly convert spectral bin model data or in situ measurement for each size bin to radar variables. This conversion facilitates the transfer of crucial information, such as mass, density, number concentration, terminal velocity, cross-sectional area, AR, and particle size distribution, without the need for further assumptions. In contrast, a bulk microphysics model provides hydrometeor mixing ratio in one-moment microphysics models (e.g., Baldauf et al., 2011) or mixing ratio and number concentration in two-moment microphysics models (e.g., Seifert and Beheng, 2006), requiring assumptions about particle size distribution, mass–size relations, and terminal velocity in PAMTRA. In the context of the spectral bin model AMPS, the terminal velocity for the sedimentation of a prognostic variable for a specific bin is determined by considering the mass, concentration, and the particular type of PPVs within that bin (Hashino and Tripoli, 2007). Radar reflectivity factor z_e ($\text{mm}^6 \text{m}^{-3}$) is obtained by integrating the normalized particle size distribution (PSD) $n(D)$ over the entire range of particle sizes D ,

$$z_e = \int 10^{18} \sigma_B(D) n(D) \frac{\lambda^4}{\pi^5 |K_w|^2} dD, \quad (1)$$

where λ is the wavelength in meters, $|K_w|$ corresponds to the dielectric factor of water, and $\sigma_B(D)$ stands for the backscattering cross-section of individual hydrometeor particles in square meters (m^2). Typically, radar reflectiv-

ity is used in logarithmic units converted with $Z_e(\text{dBZ}) = 10 \log_{10} z_e (\text{mm}^6 \text{m}^{-3})$.

It is standard practice to use the value for liquid water at centimeter wavelengths ($|K_w| = 0.93$ at Ka-band; Ulaby et al., 1981) regardless of whether ice or liquid clouds are observed. However, $|K_w|$ is also frequency dependent. This study employs the self-similar Rayleigh–Gans approximation (SSRGA) parameterization proposed by Hogan et al. (2017) for the backscattering cross-section $\sigma_B(D)$ calculation. This parameterization is determined by five dimensionless parameters: α_e , K , β , γ , and ζ . The AR of the particles is represented by α_e , whereas K measures the mean mass distribution of the particle along the propagation direction and is referred to as the kurtosis parameter. The mass fluctuations around the mean mass distribution are described by β and γ , which represent the power law prefactor and exponent, respectively. ζ is a correction term for the power spectrum of the smallest wavenumber. We choose the SSRGA coefficients depending on the normalized particle rime mass fraction following Maherndl et al. (2023).

3 Model description and simulation setup

3.1 Initial profile

We selected a one-dimensional mixed-phase stratocumulus case for our experiments with the KiD-AMPS framework. To minimize the effects of the microphysics schemes, the temperature field is kept constant. The vertical velocity demonstrates repeated up–down oscillation, and an additional vapor source is supplied to artificially recreate a quasi-steady stratocumulus condition. The vertical velocity is given as

$$w(z, t) = \begin{cases} w_1 \frac{z}{z_1} \left(1 - \exp \left[- \left(\frac{z-z_1}{z_2} \right)^2 \right] \right) \sin(\pi t/t_1), & \text{if } z < z_1 \\ 0.0, & \text{otherwise} \end{cases} \quad (2)$$

and the additional forcing

$$\frac{dq}{dt}_{\text{add}}(z, t) = \frac{dq}{dt}_{\text{add}}(z, 0) = \begin{cases} A \cos \left(\frac{1.25\pi}{2} \right), & \text{if } z < z_3 + z_4, \\ A \cos \left(\frac{z-z_3}{z_4} \frac{\pi}{2} \right), & \text{if } z_3 + z_4 < z < z_3 \\ & + 1.25z_4, \end{cases} \quad (3)$$

and A satisfies

$$\int_0^{z_5} \frac{dq}{dt}_{\text{add}}(z, 0) dz = f_q/3600. \quad (4)$$

The parameters z_1 , z_2 , z_3 , z_4 , and z_5 are set to 450, 200, 400, 100, and 1000 m, respectively. Similarly, the values of w_1 , t_1 , and f_q are set to 1.0 m s^{-1} , 600 s, and 5 mm h^{-1} , respectively. The initial potential temperature and specific humidity profile are displayed in Fig. 3. This implies that the cloud's top region exhibits a temperature of approximately -20°C , whereas the lowermost part of the cloud shows a temperature of -15°C . Importantly, the profiles were specifically crafted to emulate a mixed-phase stratocumulus layer,

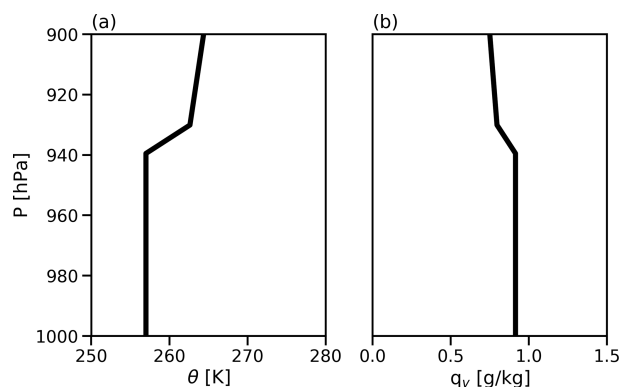


Figure 3. The initial condition of the (a) potential temperature θ (K) and (b) specific humidity q_v (g kg^{-1}) profile in the KiD-AMPS simulation.

drawing inspiration from the Global Energy and Water Cycle Experiment Cloud System Study (GCSS) Surface Heat Budget of the Arctic Ocean (SHEBA) intercomparison, a choice substantiated by previous studies (Klein et al., 2009; Morrison et al., 2011; Fridlind et al., 2012). This selection was made with the deliberate intent of aligning our study's environmental conditions with well-established benchmarks, thereby enabling seamless comparisons with other investigations centered around similar Arctic settings. The GCSS–SHEBA intercomparison is widely acknowledged for providing meticulously documented atmospheric conditions that faithfully represent Arctic stratocumulus clouds, rendering it an ideal resource for our initial profiles.

3.2 Experimental designs (CCN and INPs)

This study aimed to investigate the impact of varying initial concentrations of CCN and INPs on the formation and evolution of clouds. It is widely recognized that aerosols can significantly influence cloud formation and evolution, with their role in these processes depending on factors such as size, composition, and concentration. It should be noted that while aerosols can act as a source of INPs, not all aerosols possess this capability. INPs are particular types of particles capable of initiating ice crystal formation at temperatures below 0°C . The precise composition and physical properties of INPs can considerably vary based on specific conditions, with mineral dust, biological particles (e.g., bacteria and fungi), and certain anthropogenic particles (e.g., industrial emissions) being the most prevalent sources of INPs (Hoose and Möhler, 2012). For this research, we employ ammonium sulfate as CCN and assume that the insoluble portion of all aerosols consists of montmorillonite as INP sources. Hashino et al. (2020) demonstrated that the volume-dependent Bigg's immersion method (Diehl and Wurzler, 2004) is well suited for characterizing the ice nucleation process. Consequently, we adopt Bigg's immersion freezing method in this study as well. For further details on ice nucleation schemes, de Boer

et al. (2010, 2013) and Hashino et al. (2020) can be referred to.

Within the AMPS model, aerosol particles are represented by lognormal size distributions, which provide comprehensive coverage of their size range. In the CCN activation scheme, the particle size distribution is divided into 10 bins, and for each bin, the critical supersaturation value is individually computed. As the iteration proceeds, bins that exhibit a critical supersaturation below the threshold of environmental supersaturation are identified and subsequently transferred to the liquid spectrum. This methodology ensures the appropriate incorporation of bins in the liquid phase, leading to a faithful depiction of cloud microphysics within the AMPS model. As previously mentioned, montmorillonite particle number concentration serves as an INP proxy for this simulation. For the present study, we conduct sensitivity analyses in this study by altering CCN and INP proxy concentrations across an extensive range, from extremely low to exceptionally high levels, as illustrated in Table 2. The initial CCN concentrations for these sensitivity simulations are set at 10, 50, 500, 1000, and 5000 cm^{-3} (denoted as CCN10, CCN50, CCN500, CCN1000, and CCN5000, respectively). For each CCN condition, simulations are carried out with initial INP particle concentrations of 0.001, 0.1, and 10 L^{-1} , respectively, labeled INP0.001, INP0.1, and INP10. A similar range for the experimental setup was also selected in the sensitivity study of Fan et al. (2017). The authors further emphasize that in heavily polluted regions like China and India, where CCN concentrations exceeding 1000 cm^{-3} are prevalent, such high values hold significant implications for precipitation extremes and water cycles. Choudhury and Tesche (2023) provide a comprehensive global multiyear dataset of height-resolved concentrations of cloud condensation nuclei (CCN) categorized by aerosol types. These estimates are derived from the spaceborne lidar instrument aboard the Cloud-Aerosol Lidar and Infrared Pathfinder Satellite Observation (CALIPSO) satellite. Notably, recent studies have demonstrated that the levels of extreme CCN concentrations in heavily polluted regions can exceed 5000 cm^{-3} . The selected INP range is well motivated with respect to the variability that can be found in existing in situ and remote sensing studies of INP concentrations. Specifically, we based the decision for the lowest value of INP concentration on the values reported for the free troposphere over the Southern Ocean site of Punta Arenas, Chile (Radenz et al., 2021). The selected maximum value of INP concentration of 10 L^{-1} can, e.g., be observed in the case of strong Saharan dust outbreaks in the Mediterranean region, as reported for instance by Ansmann et al. (2019). The range also agrees well with in situ measurements, as reported by DeMott et al. (2010).

In total, we conducted 15 experiments, and from this set, we specifically selected five representative cases (EXP1–5) for detailed analysis in Sect. 4.1 of the Results section (see Table 2). These selected cases encompass clean, pristine, and polluted scenarios, achieved by varying the concentration of

Table 2. Definition of the EXP1–5 experiments referred to in the remainder of this study. The simulations are conducted using various concentrations of CCN and INP aerosols.

		CCN [cm^{-3}]				
		10	50	500	1000	5000
INP [L^{-1}]	0.001	X	EXP3	X	X	X
	0.1	EXP4	EXP2	EXP5	X	X
	10	X	EXP1	X	X	X

CCN and adjusting the concentration of INPs to be 100 times smaller and 100 times larger than the commonly observed value of 0.1 L^{-1} in Arctic mixed-phase clouds. The results of the sensitivity test, covering all cases, are presented in Sect. 4.2. Additionally, Sect 4.3 showcases the outcomes of coupling typical EXP1–5 cases with PAMTRA for radar retrieval analysis.

4 Results

4.1 Comparative analysis of CCN and INP effects on mixed-phase clouds

We analyze the evolution of cloud formations and the progression of hydrometeors by altering the initial CCN and INP concentrations. In this section, our primary focus is on cases EXP1–5 (see Table 1), which represent the most contrasting experimental scenarios among the 15 cases examined.

Figure 4 presents the temporal evolution of cloud development, specifically focusing on the average column value over time. This figure provides valuable insights into the progression of cloud formation in relation to the initial conditions, considering the variations in CCN and INPs. In Fig. 4a, we present the effective diameter values of ice particles obtained from the simulations. In this study, the effective diameter of ice particles, denoted as $D_{\text{eff,ice}}$, is calculated using Eq. (5).

$$D_{\text{eff,ice}} = 2\sqrt{V_{\text{cs}}/(\pi l_{\text{c,sm}})} \quad (5)$$

The mean effective diameters after $t = 100 \text{ min}$ for EXP1, EXP2, EXP3, EXP4, and EXP5 are 79, 293, 331, 275, and $346 \mu\text{m}$, respectively. It is observed that as the concentration of INPs increases, there is a corresponding decrease in the effective diameter of ice particles, as evident in EXP1, EXP2, and EXP3. Conversely, an increase in CCN concentration results in a slight increase in the effective diameter, as observed in EXP4 and EXP5. The simulated effective diameters of ice particles span a wide range, ranging from small values in the tens of micrometers to larger values in the range of thousands of micrometers. These findings are consistent with previous observations indicating effective diameters within the range of 300 to $800 \mu\text{m}$ (Morrison et al., 2011).

AMPS is comprised of two separate bin spectra. The first 40 bins represent the liquid phase and are categorized as ei-

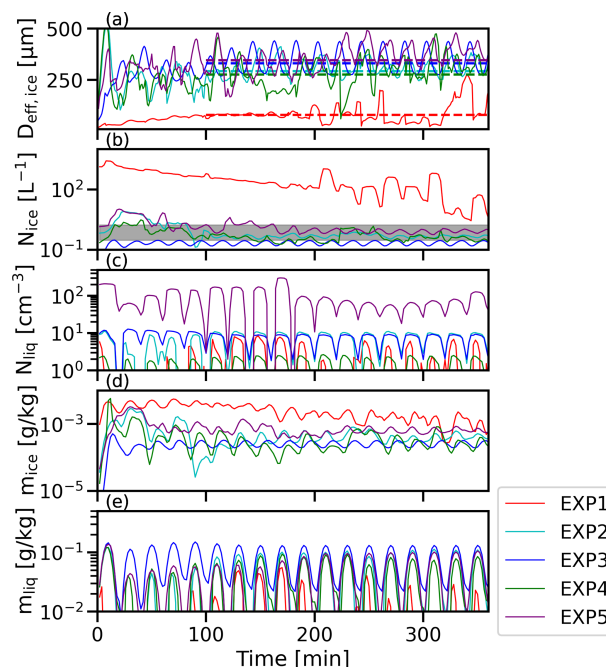


Figure 4. Time series of key variables: (a) effective diameter of ice crystals ($D_{\text{eff,ice}}$) with the dotted line representing the average value from 100 min, (b) ice number concentration (N_{ice}), (c) liquid number concentration (N_{liq}), (d) mixing ratio of ice (m_{ice}), and (e) mixing ratio of liquid (m_{liq}). The gray-shaded regions correspond to the ranges derived from observational data obtained during the SHEBA campaign.

ther cloud or rain, while the next 20 bins represent the ice phase. The mixing ratio and number concentration of liquid and ice particles are found to remain in a quasi-steady state, with the exception of EXP1. Moreover, the experimental results in Fig. 4b for the number concentration of ice (N_{ice}) in EXP2, EXP4, and EXP5, ranging from 0.3 to 1.7 L^{-1} (gray zone), are in agreement with previous observations from the SHEBA campaign of mixed-phase clouds (Morrison et al., 2011; Fridlind et al., 2012). These results further suggest that the experiment accurately represents typical mixed-phase clouds. Figure 4 indicates that as INP concentrations increase in EXP1, EXP2, and EXP3, both N_{ice} and m_{ice} significantly increase, while N_{liq} and m_{liq} decrease. Conversely, the mean m_{ice} is slightly higher in experiments with increased CCN (EXP4, EXP2, and EXP5) despite the higher N_{liq} and m_{liq} , consistent with findings from earlier studies employing two-moment bulk microphysics simulations (Solomon et al., 2018) and experimental investigations (Desai et al., 2019).

The impact of CCN and INP perturbations on cloud evolution is illustrated in Fig. 5. It is observed that increasing CCN concentration can significantly affect the relationship between liquid water and ice mixing ratios. In response to the increased concentration of INPs, the ice water content increased, as well. In the high-INP scenario (EXP1), the con-

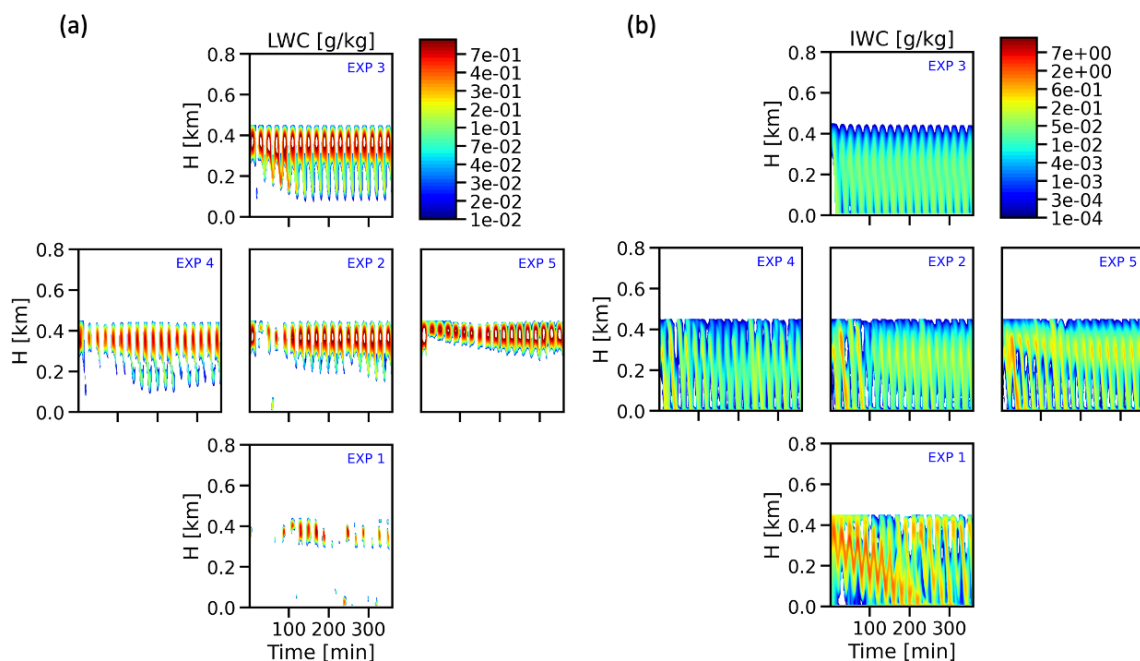


Figure 5. Vertical distribution comparison of (a) liquid water content (LWC) (g kg^{-1}) and (b) ice water content (IWC) (kg^{-1}) across EXP1–5.

version of water droplets into ice crystals occurs more rapidly and efficiently. Consequently, this case predicts almost fully glaciated clouds. When the number of CCN increases, more cloud droplets are formed from within the reservoir of available water vapor. This can lead to an increase in the number concentration of cloud droplets within the cloud as shown in Fig. 4c, which can, in turn, reduce the size of individual cloud droplets. This reduction in droplet size increases the altitude of the mixed-phase cloud base and reduces the amount of precipitation, which can result in an increase in cloud water mass, given that the cloud is not already saturated with the available water vapor. In summary, the alteration of cloud particle concentration due to perturbations in the aerosol concentrations leads to adjustments in cloud–dynamics interaction, as previously observed in studies by Seifert et al. (2012), Boucher et al. (2013), Heyn et al. (2017), Possner et al. (2017), Solomon et al. (2018), and Zhang et al. (2018).

Next, we investigate the response of the ice-phase processes of AMPS to the aerosol perturbations. In the AMPS model, the mass of an ice crystal is partitioned into various process-oriented categories, including pristine crystal mass, aggregated mass, riming mass, and melted water mass, which are tracked as PPVs. The bin components are created through microphysical processes that act upon them, including vapor deposition onto ice crystals, which produce ice crystal mass; melting processes, which produce liquid mass; aggregation processes, which generate aggregate mass; and riming processes, which produce rime mass. The sum of these

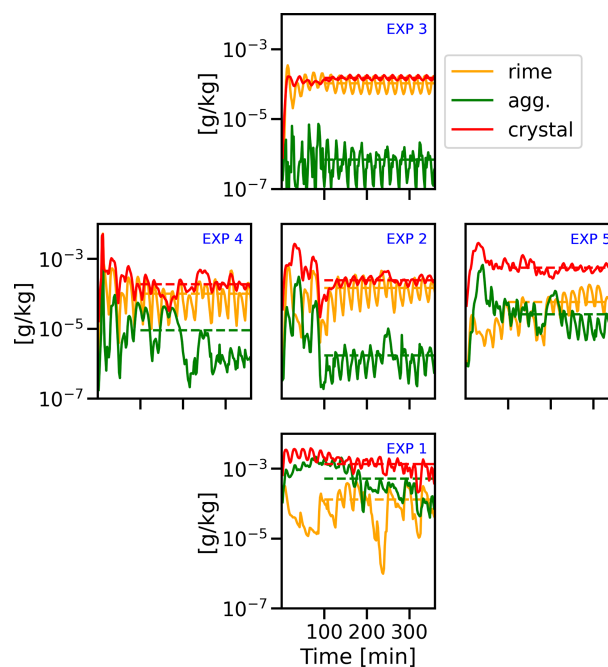


Figure 6. Temporal evolution comparison of the mean mixing ratios of ice processes with the dotted line representing the average value from 100 min, including melting, riming, aggregation, and crystal across EXP1–5. The aggregation process is abbreviated as “agg.”.

four components makes up the total mass. In Fig. 6, the mixing ratio of ice water content is presented separately for the four ice-phase processes and for each of the five selected experiments. High concentrations of INPs lead to an increased number concentration of ice particles (see Fig. 4) and consequently to increased ice water mass, as the presence of INPs allows the formation of ice crystals to occur more readily, resulting in an increased number of collisions and coalescence among the ice crystals. The results demonstrate that as the number of aerosols and concentration of INPs increase, there is a corresponding increase in the frequency of aggregation due to the higher concentration of ice crystals that promote this process. Conversely, it is observed that the occurrence of riming is reduced when there is a shortage of sustained supercooled liquid layers.

The concentration of CCN directly impacts the condensation of water vapor into liquid droplets. With an increase in CCN concentration, a greater number of smaller liquid droplets is formed. However, these smaller droplets have lower inertia and are less effective at colliding with ice particles. As a result, the efficiency of the riming process decreases as the number of small supercooled droplets increases. This observation aligns with a previous observation study conducted by Borys et al. (2003). Additionally, the persistence of smaller droplets that freeze before colliding with ice particles and before being able to contribute to riming can grow via the Bergeron–Findeisen process (Bergeron, 1935; Findeisen, 1938). This process, which operates most efficiently within the temperature range of -15 to -20 °C, occurs in mixed-phase clouds where both supercooled water droplets and ice particles coexist. In the Bergeron–Findeisen process, water vapor tends to preferentially condense onto the ice particles due to the lower saturation vapor pressure over ice compared to water. As a result, the preferential growth of ice particles leads to an increase in the number of ice particles and a decrease in riming mass. Figures 4 and 5 illustrate how elevated CCN concentrations lead to an increase in the number of ice particles, specifically EXP4 and EXP5, and a decrease in riming efficiency.

Therefore, fluctuations in CCN and INP concentrations have significant effects on precipitation formation by modifying the amount of supercooled liquid water. The results indicate that polluted clouds exhibit a reduced size and higher amounts of supercooled liquid water, resulting in precipitation preferably formed through ice-phase aggregation rather than riming processes. Conversely, pristine clouds characterized by a larger size and lower amounts of supercooled liquid water predominantly generate precipitation through riming processes.

The frequency of ice particle freezing is influenced by the sizes of liquid particles that freeze most frequently in each scenario. The parameterization of immersion freezing takes into account the volume of the droplets, indicating that larger droplets have a higher probability of freezing. However, the number concentration of the droplets also plays a role, with

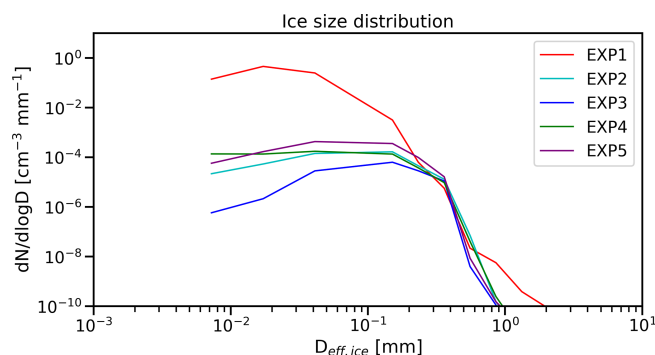


Figure 7. The mean ice particle size distribution averaged after $t = 100$ min.

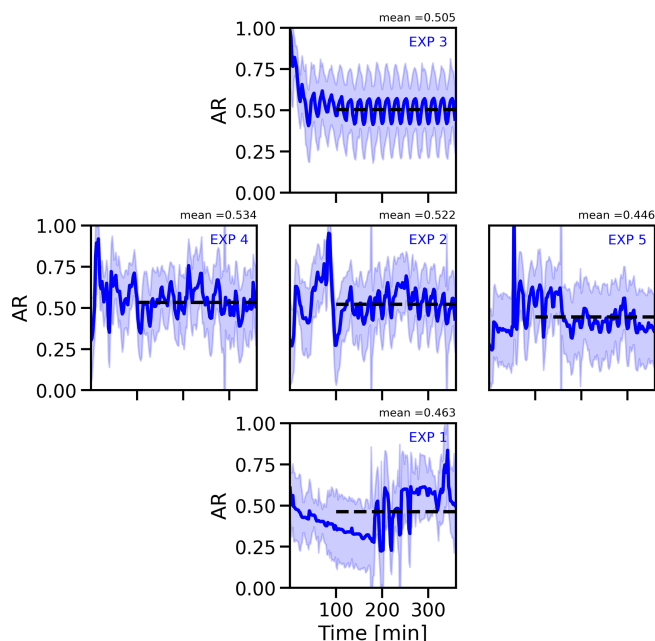


Figure 8. Comparison of the temporal evolution of the mean aspect ratio (AR) with the dotted black line representing the average value from 100 min across EXP1–5.

smaller droplets being more prevalent. Consequently, drawing definitive conclusions about the overall effect becomes challenging. Figure 7 illustrates the size distribution of ice particles based on number weighting. The results demonstrate that an increased concentration of INPs corresponds to a significant abundance of small ice particles. When comparing EXP1 and EXP2, it is worth highlighting that despite EXP1 showing a smaller average size, it still exhibits a substantial population of small particles. This is further compounded by the aggregation process, which plays a pivotal role in transforming these initially smaller hydrometeors into relatively larger ice particles.

In this study, Fig. 8 presents the correlation between the number-weighted AR of ice particles and the concentrations of INPs and CCN in mixed-phase clouds. Notably, the re-

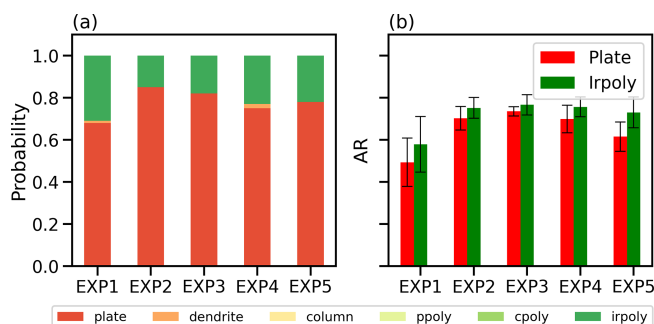


Figure 9. Comparative analysis of the probability of (a) ice habit classification, including plate, dendrite, column, planar polycrystal (ppoly), columnar polycrystal (cpoly), and irregular polycrystals (irpoly), and (b) mean AR and standard deviation (with error bars) for plate and irregular polycrystals during the 2 h period following 100 min across EXP1–5.

sults indicate that regardless of the conditions, the ice particles exhibit an oblate-like shape with a specific AR within the temperature range from -20 to -16 °C. Furthermore, the AR decreases as the INP concentration increases. This is attributed to the fact that higher INP concentrations promote the formation of smaller and more compact ice crystals with extreme ARs, in contrast to larger crystals that develop in low-INP environments. The smaller-sized crystals exhibit a more pronounced AR due to the non-linear feedback ($\frac{dl_c}{dl_a} = \Gamma(T)l_c/l_a$), where Γ represents the inherent growth ratio of ice crystals, reflecting the current atmospheric conditions and the change in the mass of the ice particle (Chen and Lamb, 1994; Hashino and Tripoli, 2007; Hashino et al., 2020).

Similarly, in the scenario with low CCN concentration (EXP4), ice particles undergo growth through the deposition and riming process, resulting in more spherical shapes. Conversely, in the high-CCN scenario, the freezing of droplets through the immersion mode occurs at smaller sizes, leading to the nucleation of smaller ice crystals and the subsequent formation of smaller ice particles. When comparing EXP4 and EXP5 in Fig. 7, an increase in CCN concentration is observed to coincide with a significant rise in the concentration of smaller ice particles, accompanied by a decrease in the abundance of larger ice particles around 1 mm. Consequently, the overall average value exhibits a decreasing trend with increasing CCN concentration, primarily driven by the greater number of small ice particles. This phenomenon also leads to an increase in ice water mass and the availability of water vapor for ice particle growth, resulting in a higher abundance of small ice particles and a slight decrease in the AR, as illustrated in Fig. 8.

To gain a better understanding of the AR, we examined the AR with each ice habit in detail. As shown in Fig. 9, the ice particles in the mixed-phase clouds, where the temperature ranges from -20 to -16 °C, primarily exhibit an oblate-

like shape with AR (α) < 1, consisting of plates and irregular polycrystal habits. The result agrees with earlier findings from laboratory studies (Bailey and Hallett, 2009) and observations (Auer and Veal, 1970). Most droplets that freeze close to -20 °C are polycrystalline in nature, as observed in polycrystalline ice habit frequency from in situ observations (Bailey and Hallett, 2009).

To clarify, in the AMPS model, if the maximum dimension of the ice crystal is less than 20 μm and the temperature is below -20 °C, the growth regime is determined using the corresponding cumulative relative frequency of habits and a random number generator. In this case, small ice crystals can exhibit growth modes that differ from the habit diagnosed at the start of the time step. However, for temperatures above -20 °C, it is assumed that polycrystals do not form. Once the maximum dimension of the ice crystal exceeds 20 μm , it is assumed to follow the growth of the diagnosed habit at the beginning of the time step. This indicates that most irregular polycrystals observed in this experiment primarily formed within the initial cloud top layer, where temperatures are near -20 °C. The result is consistent with the findings of Hashino et al. (2020).

Figure 9a provides insights into the predominant shape of ice particles, with plates representing the majority of the particles. EXP1 exhibits a plate fraction of 68 %, while the remaining experiments range from 75 % to 85 %. As the concentration of INPs increases, a greater number of ice particles forms, as shown in Fig. 4. Over time, the initially formed plate-shaped ice crystals undergo a transformation influenced by the aggregation process, resulting in the emergence of irregular polycrystals. Notably, the AR of plates gradually decreases compared to that of irregular polycrystals as the INP concentration increases. In EXP1, as depicted in Fig. 8, the AR demonstrates an increase after 200 min, primarily attributed to the formation of irregular polycrystals. This phenomenon arises from the aggregation process involving newly formed small ice particles and pre-existing ice particles. The resulting irregular polycrystals exhibit a higher AR compared to the plate-shaped crystals, contributing to an overall increase in the average AR. In EXP1, the aggregation process becomes more pronounced, leading to the formation of fully glaciated clouds and a notable increase in the occurrence of irregular polycrystals. A comparison between EXP4 and EXP5 in Fig. 9a reveals similar proportions of the plate and irregular polycrystal shapes. However, Fig. 9b shows that the AR is smaller in EXP5. This observation is consistent with previous results, indicating that higher concentrations of CCN lead to higher ice particle concentrations, resulting in a lower AR.

In conclusion, Fig. 9 provides compelling evidence of a correlation between the concentration of INPs, CCN, and the AR of ice particles. The findings indicate a decrease in the AR as the concentrations of INPs and CCN increase.

4.2 Sensitivity test

In Sect. 4.1 of this study, the primary focus is the analysis and comparison of the five most frequently observed scenarios, exploring the changes observed over the entire duration of the experiment. Now, in Sect. 4.2, the focus shifts to examining the average values, specifically excluding the initial 100 min for each experiment. The objective of this section is to investigate the tendencies and influences of individual ice microphysical processes, as well as to assess the impacts of varying dynamics and initial INP types across a total of 15 setups.

Figure 10 illustrates the mean freezing rate of ice particles under different CCN and INP scenarios. In the AMPS model, the source terms of ice mass include ice nucleation, vapor deposition, aggregation, riming, hydrodynamic breakup, and melting–shedding. In mixed-phase clouds, ice particles primarily grow through vapor deposition, a process in which water vapor molecules freeze onto their surface. According to the experiments, deposition is the primary process for ice growth, further enhanced by increasing CCN and INP concentrations. The riming and aggregation processes are the next significant contributors, followed by the nucleation process. The hydrodynamic breakup and melting–shedding processes are not activated in this experiment.

The increase in INP concentration amplifies the contact nucleation process, aggregation process, and subsequent depositional growth, while the riming-related growth and immersion nucleation process show a decline. At low INP concentrations, the riming-related growth is comparable to deposition. However, as the INP concentration rises, the contribution of riming diminishes considerably, as discussed earlier. Consequently, the availability of liquid becomes a limiting factor for riming. The contribution of riming exhibits a significant decrease with increasing CCN concentration, except in low-INP conditions. Notably, when a substantial difference exists, the difference can exceed 10 times the values observed in between different scenarios. The major microphysical processes, including vapor deposition, riming, and nucleation, exhibit high sensitivity to INPs. Their sensitivity becomes more significant in high-INP conditions, accompanied by significant changes in dynamics and thermodynamics. To investigate the impact of dynamic factors, we decreased w_1 from 1.0 to 0.5 m s^{-1} in Eq. (2), leveraging the capability of KiD-AMPS to differentiate between dynamic and microphysical effects. The results confirm that an increase in w_1 amplifies the vapor deposition rate, aggregation rate, and contact nucleation processes while reducing the immersion freezing rate. However, the overall trends exhibit a similar pattern.

According to Hashino et al. (2020), the volume-dependent Bigg's immersion method (Diehl and Wurzler, 2004) is a suitable approach for modeling mixed-phase clouds (see Eq. 1 in Hashino et al., 2020). To account for this information, we adapt Bigg's immersion freezing scheme for our

study. In this scheme, the freezing rate is strongly influenced by the droplet mass as well as Bh and temperature. Bh represents the freezing efficiency of insoluble material in the droplet and is currently set to $3.2 \times 10^{-5} \text{ cm}^{-3}$ for montmorillonite, as reported by Diehl and Wurzler (2004). To explore the effects of varying Bh, we multiplied the parameter by a factor of 10 and compared the resulting changes in freezing rates. The findings are presented in Fig. 11, indicating that an increase in Bh results in an increase in immersion freezing rate, aggregation production rate, and a minor increase in vapor deposition rate, while the effect of contact nucleation decreases. Nonetheless, the vapor deposition process remains the dominant factor, impacting the AR by reducing it as Bh increases. This is similar to the effect of INP increase, which generates smaller AR. The prominence of this effect can be attributed to the enhanced production of small droplets, as depicted in Fig. 7.

The relationship between CCN concentration and the rate of ice production through immersion freezing in mixed-phase clouds is complex and depends on multiple factors. In theory, an increase in CCN concentration can result in the formation of more cloud droplets. If these droplets become supercooled, they can potentially serve as sites for ice formation through immersion freezing when INPs are present. This suggests a potential increase in the rate of ice production with higher CCN concentration. However, the results reveal a decrease in the contribution of immersion nucleation with increasing CCN concentration. This can be attributed to the twofold effect of increasing CCN. On the one hand, it can lead to a higher number of cloud droplets available for freezing. On the other hand, it tends to produce smaller cloud droplets due to increased competition for available water vapor, known as the Twomey effect (Twomey, 1974). Smaller droplets require colder temperatures to freeze, making them less likely to initiate ice formation. As a result, an increase in CCN concentration does not lead to a corresponding increase in the rate of ice production if the droplets are too small to freeze. Moreover, as the concentration of INP increases, the mass contribution of the immersion freezing rate also decreases. As depicted in Fig. 5, an increase in INP concentration leads to a decrease in LWC, as well as a reduction in the areas of ice particles and coexistence. The immersion freezing rate is influenced by the average mass of droplets in the same mass bin and location. Therefore, it is evident that the immersion freezing rate also declines with increasing INP concentrations.

To sum up, the relationship between aerosol concentration and the rate of ice production through immersion freezing is intricate and influenced by various factors, including the properties and concentration of CCN and INPs, temperature, and supersaturation level within the cloud. To definitively determine the actual effect of increasing INPs and CCN on the rate of ice production through contact freezing and immersion freezing, careful cloud microphysical modeling or observations are necessary.

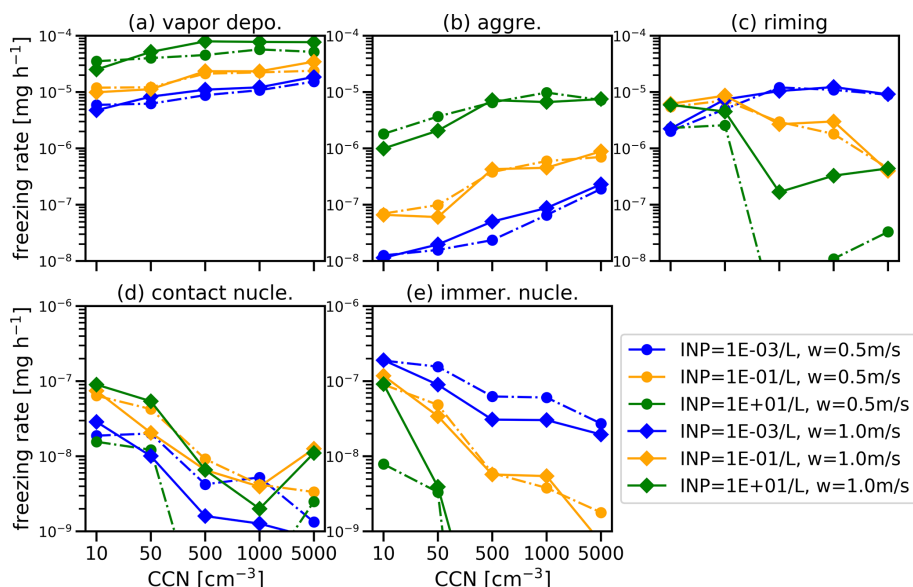


Figure 10. Comparison of mean freezing process rates, including (a) vapor deposition, (b) aggregation, (c) riming, (d) contact nucleation, and (e) immersion nucleation across 15 cases. The model outputs for the process rates are recorded every 1 min, and the data are spatially averaged over the domain grid points, excluding the first 100 min. The dashed line represents the value of w_1 when we decrease from 1.0 to 0.5 m s^{-1} , as defined in Eq. (2).

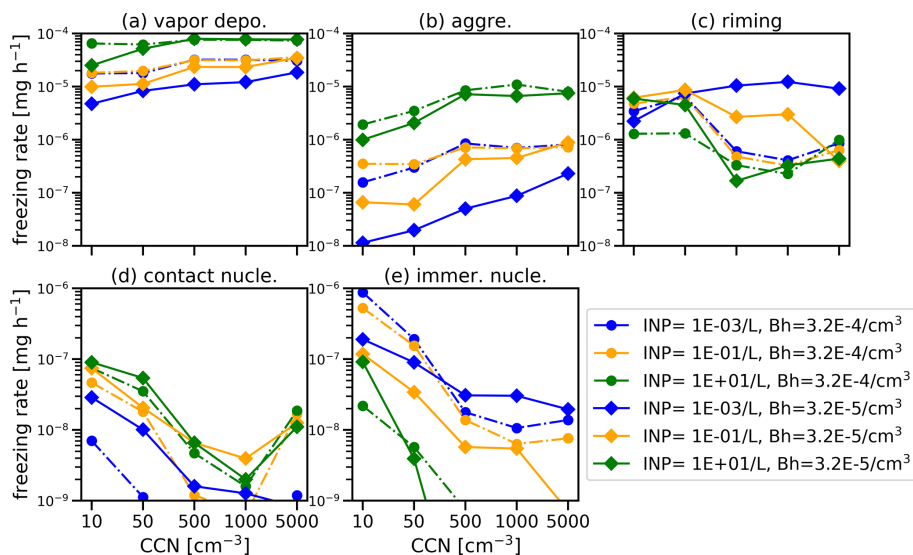


Figure 11. Comparison of the mean freezing process rates, including vapor deposition, riming, contact nucleation, and immersion nucleation, across 15 cases. The data presented in the plots were processed using the same methodology as described in Fig. 10. The dashed line in the plots represents the enhanced value of the immersion freezing rate ($B_h = 3.2 \times 10^{-4} \text{ cm}^{-3}$) as defined in Eq. (1) in the study by Hashino et al. (2020).

4.3 PAMTRA coupled with AMPS

In this final result section, the application of PAMTRA to the EXP1–5 simulations is elaborated on to demonstrate the sensitivity of radar observations to changes in CCN and INPs.

As radar reflectivity is determined by multiple parameters, including size, density, and AR (see Eq. 1), forward simulations are required in order to evaluate the effects of INP

and CCN perturbations on observable parameters such as the radar reflectivity. The results of the forward simulations for the five experiments, as explained in Sect. 2.3, are shown in Fig. 12. The spectral bin model reveals a clear decrease in particle size as aerosol loads increase, which leads to a decrease in radar reflectivity due to the strong dependence of backscattering on particle size to the power of 6. How-

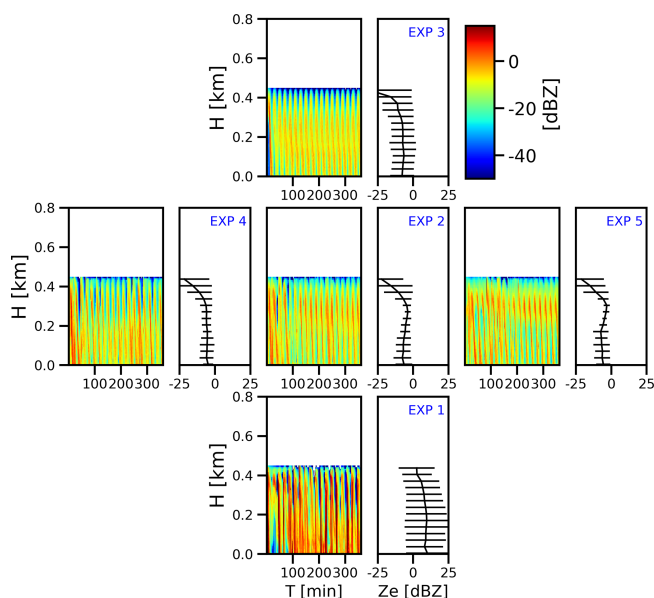


Figure 12. Comparison of the distribution and mean vertical profile of the forward-modeled radar reflectivity factor Z_e (dBZ) at Ka-band using the PAMTRA across EXP1–5.

ever, as shown in Fig. 12, the radar reflectivity increases with increasing INP concentrations, which is consistent with observations (Zhang et al., 2018; Radenz et al., 2021). The increase in reflectivity is attributed not only to changes in particle size but also to alterations in number concentration, AR, and other parameters.

In the context of analyzing radar reflectivity data, it is essential to determine the mean vertical profile in order to understand the atmospheric structure and characteristics at various altitudes. This information provides valuable insights into the vertical distribution of hydrometeors. Examining the profiles in Fig. 12, we observe a noticeable increase in reflectivity at the cloud bottom (at around 300 m) as the CCN concentration rises. This increase can be attributed to the greater number of cloud droplets resulting from the higher CCN concentration. It is noteworthy that EXP5 displays a remarkably low standard deviation in the cloud bottom at 300 m, indicating a relatively uniform distribution of particle sizes in that region. Consistent with expectations, an increase in the INP concentration leads to elevated reflectivity across different altitude levels, accompanied by an increased standard deviation. Higher mean reflectivity values in EXP1 show a larger abundance of hydrometeors in the observed scenarios. However, an intriguing finding is the contrasting pattern observed in the cloud top, where the standard deviation demonstrates a decrease.

Table 3 presents the comprehensive statistics of reflectivity, detailing the total (temporal and vertical) mean (μ), standard deviation (σ), and skewness (\bar{M}). Our examination of radar reflectivity data unveils distinct statistical patterns that are influenced by the concentrations of CCN and

INPs. For instance, we find that the mean radar reflectivity is -10.09 dBZ, accompanied by a standard deviation of 5.60 dBZ and a skewness of 1.19 for the reference mixed-phase stratocumulus cloud case in EXP2. These values indicate a relatively symmetrical distribution with a slight rightward skew. As the CCN concentration increases while maintaining the same INP level in EXP5, we observe a marginal rise in the mean reflectivity to -9.87 dBZ, a decrease in the standard deviation to 5.0 dBZ, and an increase in the skewness to 1.71 , suggesting a more pronounced skewness in the distribution.

On the other hand, where the INP concentration is elevated to 10 L^{-1} at a CCN concentration of 50 cm^{-3} in EXP1, we note a significant increase in the mean reflectivity to 4.65 dBZ, a larger standard deviation of 12.47 dBZ, and a substantially higher skewness of 2.87 . These findings signify a more dispersed and highly skewed distribution, possibly indicating the presence of different hydrometeor types and size variations, including precipitation particles. In this study, this is linked to the aggregation of ice particles. Hydrometeors are plate and irregular polycrystals, most of which are plates. However, as depicted in Fig. 7, the size distribution of ice particles is quite diverse in EXP1. Conversely, when the INP concentration is very low at 0.001 L^{-1} while maintaining a CCN concentration of 50 cm^{-3} , the mean radar reflectivity measures -11.83 dBZ, the standard deviation is 9.12 dBZ, and the skewness is 0.36 , implying a homogeneous distribution with a slight leftward skew and a low number of ice and liquid particles. Comparing the mean Z values between EXP2 and EXP3 shows minimal differences. However, distinct variations in distribution are observed based on the values of σ and \bar{M} .

5 Summary and conclusions

This study examines how perturbations in CCN and INP concentrations affect the shape of ice particles in mixed-phase clouds. The results reveal that both CCN and INP concentrations play a vital role in determining the shape of ice particles and influencing cloud microphysics. The effective diameter of ice particles, which indicates their size, is found to be influenced by the concentrations of CCN and INPs. Higher INP concentrations result in smaller effective diameters, while increased CCN concentrations lead to a slight increase in size. The size distribution of ice particles ranges from tens of micrometers to thousands of micrometers, consistent with previous observations. Analysis of the ice particle shapes shows that oblate-like crystal shapes are most common in the temperature range from -20 to -16 °C. However, a significant presence of irregular polycrystals is observed, especially in scenarios with high INP concentrations. In scenarios with high INP concentrations, we observe a complex interplay of nucleation, aggregation, and collision phenomena. These occur against a backdrop of dynamic changes in cloud stabil-

Table 3. Statistical analysis of the radar reflectivity factor (Z_e) (dBZ) distribution, which includes the computation of mean (μ), standard deviation (σ), and skewness (\tilde{M}) values. The data are spatially averaged over the grid points of the domain, excluding the initial 100 min.

(μ, σ, \tilde{M})	CCN (cm^{-3})		
	10	50	500
0.001		EXP3 (−11.83, 9.12, 0.36)	
INP (L^{-1})	0.1	EXP2 (−10.09, 5.60, 1.19)	EXP5 (−9.87, 5.05, 1.71)
	10	EXP4 (−10.23, 5.70, 1.63)	EXP1 (4.65, 12.47, 2.87)

ity and limited LWC. Collectively, these processes lead to a broader distribution of ice particle sizes, ranging from larger to smaller, a pattern that is corroborated by our experimental data. The AR of ice particles is affected by both CCN and INP concentrations, with higher concentrations leading to smaller AR values. This indicates that the concentrations of CCN and INPs have an impact on the growth and shape of ice particles in mixed-phase clouds. The relationship between CCN concentration and ice particle shape is more complex than that of INPs. Increased CCN concentrations promote the formation of more cloud droplets but result in smaller droplet sizes. As a result, the efficiency of the riming process, where supercooled droplets collide with ice particles, decreases with higher CCN concentrations. In conclusion, the concentrations of CCN and INPs significantly influence the shape and morphology of ice particles in mixed-phase clouds. Higher INP concentrations lead to smaller and more compact ice particles, while increased CCN concentrations result in a decrease in the AR of ice particles. These findings highlight the intricate connection between aerosol concentrations, microphysical processes, and ice particle shapes in cloud systems. Accurate modeling and prediction of cloud behavior and precipitation require a comprehensive understanding of these relationships.

In our study, we employed the radar forward simulator PAMTRA to analyze simulation results and derive radar variables, uncovering significant disparities in the findings. When INP concentrations are at low to moderate levels, the mean value of Z_e remains relatively consistent, indicating a stable trend. However, distinct variations are observed in the Z_e distributions characterized by μ , σ , and skew \tilde{M} . Therefore, for future observational studies investigating the impact of aerosols on mixed-phase clouds, it is important to consider incorporating Z_e variability, under the condition that the actual cloud conditions align with the assumptions made in our model. In scenarios with substantial differences in INP concentrations, we observed discrepancies of 5.5 dB. This finding aligns with the results reported by Radenz et al. (2021), where a difference of 5–10 dB was observed between continental (Leipzig) and pristine (Punta Arenas) locations within specific temperature ranges. Furthermore, their study reveals that the disparity in INP concentrations is at least 1 order of magnitude higher and has the potential to be even greater if

the contribution of continental aerosols in Punta Arenas is lower than the maximum assumed value.

The formation of ice crystals with different ARs has been linked to variations in CCN and INP concentrations. However, it is important to acknowledge that factors such as temperature, humidity, and wind shear can also have a significant influence on ice crystal ARs (Barrett and Hoose, 2023). Additionally, the choice of modeling schemes can introduce sensitivity to these ratios. Interestingly, our findings show a decrease in AR with increasing INP concentration, which contradicts the results of a previous study by Ong et al. (2022) where an increase in Bh led to an increase in AR. Ong et al. (2022) also discussed the formation of columnar crystals with an AR greater than 1, which they attributed to slight variations in temperature conditions. Consequently, the AR varied as the INP concentration increased. Moreover, the occurrence of irregular polycrystals at approximately the 200 min mark highlights the intricate interplay between the initial conditions, dynamics, and microphysics of the simulation in the high-INP case. This particular timing, which is unique to our experiment, demonstrates the susceptibility of ice particle formation processes to different conditions. It is noteworthy that, given the consistent vertical wind and humidity conditions established in our simulation, extending the duration would likely result in the persistence of observed cyclical AR patterns rather than a stabilization of AR values. The complex relationship between ice particle shape and aerosol load is still not fully understood, and further research is needed to unravel the underlying mechanisms governing ice crystal formation and ARs in different environmental contexts.

The research employed the KiD model to investigate cloud microphysics processes, but it is important to consider the limitations of this one-dimensional framework. The simplified nature of the model may not fully capture the complexities and interactions observed in real three-dimensional cloud systems. Additionally, focusing solely on individual microphysical processes within the model might overlook potential uncertainties that arise from their interactions within larger-scale weather models. It is crucial to interpret the findings of this study while recognizing the limitations of the models used, including the omission of key processes such as radiation. The KiD model was developed to understand microphysics schemes without the inclusion of dynamic or radia-

tive feedbacks, which play a significant role in cloud layer heating, cooling, and their impact on cloud microphysics and dynamics. Neglecting these processes could lead to inaccuracies in the representation of cloud temperature, water vapor distribution, and vertical motions within mixed-phase clouds.

To address these limitations, future research will explore shape-integrated simulation model AMPS coupled with three-dimensional dynamic cores such as the ICOSahedral Non-hydrostatic (ICON; Zängl et al., 2015) modeling framework. The simulation data can then be compared to observational radar data using a radar forward simulator, selecting an observation dataset from field experiments. By incorporating more sophisticated tools and remote sensing techniques, a more comprehensive and accurate analysis of cloud behavior can be achieved. The aim is to enhance cloud simulations by incorporating these processes to improve realism and accuracy. Furthermore, there is a pressing need for future experiments that address a more detailed distribution of INP and CCN perturbations. Such studies aim to deepen our understanding of the dynamics of aerosol–cloud interactions. This entails evaluating how aerosol perturbations influence the evolution of idealized stratiform mixed-phase clouds, a necessary step before a precise general assessment of aerosol–cloud interactions can be realized. Such efforts will be instrumental in improving the realism and accuracy of cloud simulations by incorporating sophisticated modeling and remote sensing techniques, thereby enhancing our ability to predict cloud behavior and its implications for the climate accurately.

Code and data availability. The base code for the KiD model is publicly accessible via GitHub (<https://github.com/Adehill/KiD-A>, Hill, 2023). The AMPS codes used in this study can be obtained from the corresponding author. Simulation results are available at <https://doi.org/10.5281/zenodo.8257078> (Lee et al., 2023).

Author contributions. JL conducted all simulations, analyzed the data, and wrote the manuscript draft. JL, PS, and OK contributed initial ideas and designed experiments. PS and TH supervised the work and revised the paper. TH provided the AMPS, MM provided the PAMTRA code, and both provided support throughout the work. All authors actively collaborated in the development of the paper and participated in scientific discussions.

Competing interests. The contact author has declared that none of the authors has any competing interests.

Disclaimer. Publisher's note: Copernicus Publications remains neutral with regard to jurisdictional claims made in the text, published maps, institutional affiliations, or any other geographical representation in this paper. While Copernicus Publications makes every effort to include appropriate place names, the final responsibility lies with the authors.

Special issue statement. This article is part of the special issue “Fusion of radar polarimetry and numerical atmospheric modelling towards an improved understanding of cloud and precipitation processes (ACP/AMT/GMD inter-journal SI)”. It is not associated with a conference.

Acknowledgements. We acknowledge the support of the DFG priority program SPP 2115 PROM (project no. 359922472) and the provision of additional funding by SPP 2115 for a research stay of Junghwa Lee in Japan, which enabled the initial cooperation with Tempei Hashino, the key developer of AMPS, for the provision of training in using AMPS. We thank Tempei Hashino for hosting Junghwa Lee at his institution.

Financial support. This research has been supported by the Deutsche Forschungsgemeinschaft (grant no. 40802749), the Japan Society for the Promotion of Science Grant-in-Aid for Scientific Research (C) (grant no. JP21K03665), and by the European Commission (grant no. 101137639).

The publication of this article was funded by the Open Access Fund of the Leibniz Association.

Review statement. This paper was edited by Tuukka Petäjä and reviewed by two anonymous referees.

References

- Andrejczuk, M., Grabowski, W. W., Reisner, J., and Gadian, A.: Cloud-aerosol interactions for boundary layer stratocumulus in the Lagrangian cloud model, *J. Geophys. Res.*, 115, D22214, <https://doi.org/10.1029/2010JD014248>, 2010.
- Ansmann, A., Mamouri, R.-E., Bühl, J., Seifert, P., Engelmann, R., Hofer, J., Nisantzi, A., Atkinson, J. D., Kanji, Z. A., Sierau, B., Vrekoussis, M., and Sciare, J.: Ice-nucleating particle versus ice crystal number concentration in altocumulus and cirrus layers embedded in Saharan dust: a closure study, *Atmos. Chem. Phys.*, 19, 15087–15115, <https://doi.org/10.5194/acp-19-15087-2019>, 2019.
- Arabas, S., Jaruga, A., Pawlowska, H., and Grabowski, W. W.: libcloudph++ 1.0: a single-moment bulk, double-moment bulk, and particle-based warm-rain microphysics library in C++, *Geosci. Model Dev.*, 8, 1677–1707, <https://doi.org/10.5194/gmd-8-1677-2015>, 2015.
- Atkinson, J. D., Murray, B. J., Woodhouse, M. T., Whale, T. F., Baustian, K. J., Carslaw, K. S., Dobbie, S., O'Sullivan, D., and Malkin, T. L.: The importance of feldspar for ice nucleation by mineral dust in mixed-phase clouds, *Nature*, 498, 355–358, <https://doi.org/10.1038/nature12278>, 2013.
- Auer, A. H. and Veal, D. L.: The Dimension of Ice Crystals in Natural Clouds, *J. Atmos. Sci.*, 27, 919–926, [https://doi.org/10.1175/1520-0469\(1970\)027<0919:TDOICI>2.0.CO;2](https://doi.org/10.1175/1520-0469(1970)027<0919:TDOICI>2.0.CO;2), 1970.
- Bailey, M. P. and Hallett, J.: A Comprehensive Habit Diagram for Atmospheric Ice Crystals: Confirmation from the Laboratory,

- AIRS II, and Other Field Studies, *J. Atmos. Sci.*, 66, 2888–2899, <https://doi.org/10.1175/2009JAS2883.1>, 2009.
- Baldauf, M., Seifert, A., Förstner, J., Majewski, D., Raschendorfer, M., and Reinhardt, T.: Operational convective-scale numerical weather prediction with the COSMO model: Description and sensitivities, *Mon. Weather Rev.*, 139, 3887–3905, <https://doi.org/10.1175/MWR-D-10-05013.1>, 2011.
- Barrett, A. I. and Hoose, C.: Microphysical Pathways Active Within Thunderstorms and Their Sensitivity to CCN Concentration and Wind Shear, *J. Geophys. Res.-Atmos.*, 128, e2022JD036965, <https://doi.org/10.1029/2022JD036965>, 2023.
- Barthlott, C. and Hoose, C.: Aerosol Effects on Clouds and Precipitation over Central Europe in Different Weather Regimes, *J. Atmos. Sci.*, 75, 4247–4264, <https://doi.org/10.1175/JAS-D-18-0110.1>, 2018.
- Bergeron, T.: On the physics of clouds and precipitation, in: *Procès Verbaux de l'Association de Meteorologie*, Int. Union of Geodesy and Geophys., Paris, 156–178, 1935.
- Bony, S., Stevens, B., W Frierson, D. M., Jakob, C., Kageyama, M., Pincus, R., Shepherd, T. G., Sherwood, S. C., Pier Siebesma, A., Sobel, A. H., Watanabe, M., and Webb, M. J.: Clouds, circulation and climate sensitivity, *Nat. Geosci.*, 8, 261–268, <https://doi.org/10.1038/NCEO2398>, 2015.
- Borys, R. D., Lowenthal, D. H., Cohn, S. A., and Brown, W. O.: Mountaintop and radar measurements of anthropogenic aerosol effects on snow growth and snowfall rate, *Geophys. Res. Lett.*, 30, 1538, <https://doi.org/10.1029/2002gl016855>, 2003.
- Boucher, O., Randall, D., Artaxo, P., Bretherton, C., Feingold, G., Forster, P., Kerminen, V.-M., Kondo, Y., Liao, H., Lohmann, U., Rasch, P., Satheesh, S. K., Sherwood, S., Stevens, B., and Zhang, X. Y.: Clouds and aerosols, Cambridge University Press, Cambridge, UK, 571–657, <https://doi.org/10.1017/CBO9781107415324.016>, 2013.
- Chen, J. and Liu, Y.: New understanding and quantification of the regime dependence of aerosol-cloud interaction for studying aerosol indirect effects, *Geophys. Res. Lett.*, 43, 1780–1787, 2016.
- Chen, J.-P. and Lamb, D.: The Theoretical Basis for the Parameterization of Ice Crystal Habits: Growth by Vapor Deposition, *J. Atmos. Sci.*, 51, 1206–1222, [https://doi.org/10.1175/1520-0469\(1994\)051<1206:TTBFTP>2.0.CO;2](https://doi.org/10.1175/1520-0469(1994)051<1206:TTBFTP>2.0.CO;2), 1994.
- Choudhury, G. and Tesche, M.: A first global height-resolved cloud condensation nuclei data set derived from spaceborne lidar measurements, *Earth Syst. Sci. Data*, 15, 3747–3760, <https://doi.org/10.5194/essd-15-3747-2023>, 2023.
- Cotton, W. R., Bryan, G. H., and van den Heever, S. C.: *Storm and Cloud Dynamics*, Academic Press, ISBN 978-1483299969, 2013.
- de Boer, G., Hashino, T., and Tripoli, G. J.: Ice nucleation through immersion freezing in mixed-phase stratiform clouds: Theory and numerical simulations, *Atmos. Res.*, 96, 315–324, <https://doi.org/10.1016/j.atmosres.2009.09.012>, 2010.
- de Boer, G., Hashino, T., Tripoli, G. J., and Eloranta, E. W.: A numerical study of aerosol influence on mixed-phase stratiform clouds through modulation of the liquid phase, *Atmos. Chem. Phys.*, 13, 1733–1749, <https://doi.org/10.5194/acp-13-1733-2013>, 2013.
- DeMott, P. J., Prenni, A. J., Liu, X., Kreidenweis, S. M., Petters, M. D., Twohy, C. H., Richardson, M. S., Eidhammer, T., and Rogers, D. C.: Predicting global atmospheric ice nuclei distributions and their impacts on climate, *P. Natl. Acad. Sci. USA*, 107, 11217–11222, <https://doi.org/10.1073/pnas.0910818107>, 2010.
- Desai, N., Chandrakar, K. K., Kinney, G., Cantrell, W., and Shaw, R. A.: Aerosol-Mediated Glaciation of Mixed-Phase Clouds: Steady-State Laboratory Measurements, *Geophys. Res. Lett.*, 46, 9154–9162, <https://doi.org/10.1029/2019GL083503>, 2019.
- Diehl, K. and Wurzler, S.: Heterogeneous drop freezing in the immersion mode: Model calculations considering soluble and insoluble particles in the drops, *J. Atmos. Sci.*, 61, 2063–2072, [https://doi.org/10.1175/1520-0469\(2004\)061<2063:HDFITI>2.0.CO;2](https://doi.org/10.1175/1520-0469(2004)061<2063:HDFITI>2.0.CO;2), 2004.
- Dziekan, P., Waruszewski, M., and Pawlowska, H.: University of Warsaw Lagrangian Cloud Model (UWLCM) 1.0: a modern large-eddy simulation tool for warm cloud modeling with Lagrangian microphysics, *Geosci. Model Dev.*, 12, 2587–2606, <https://doi.org/10.5194/gmd-12-2587-2019>, 2019.
- Engelmann, R., Ansmann, A., Ohneiser, K., Griesche, H., Radenz, M., Hofer, J., Althausen, D., Dahlke, S., Maturilli, M., Veselovskii, I., Jimenez, C., Wiesen, R., Baars, H., Bühl, J., Gebauer, H., Haarig, M., Seifert, P., Wandinger, U., and Macke, A.: Wildfire smoke, Arctic haze, and aerosol effects on mixed-phase and cirrus clouds over the North Pole region during MO-SAiC: an introduction, *Atmos. Chem. Phys.*, 21, 13397–13423, <https://doi.org/10.5194/acp-21-13397-2021>, 2021.
- Fan, J., Leung, L. R., DeMott, P. J., Comstock, J. M., Singh, B., Rosenfeld, D., Tomlinson, J. M., White, A., Prather, K. A., Minnis, P., Ayers, J. K., and Min, Q.: Aerosol impacts on California winter clouds and precipitation during CalWater 2011: local pollution versus long-range transported dust, *Atmos. Chem. Phys.*, 14, 81–101, <https://doi.org/10.5194/acp-14-81-2014>, 2014.
- Fan, J., Leung, L. R., Rosenfeld, D., and DeMott, P. J.: Effects of cloud condensation nuclei and ice nucleating particles on precipitation processes and supercooled liquid in mixed-phase orographic clouds, *Atmos. Chem. Phys.*, 17, 1017–1035, <https://doi.org/10.5194/acp-17-1017-2017>, 2017.
- Findeisen, W.: Kolloid-meteorologische Vorgänge bei Neiderschlagsbildung, *Meteorol. Z.*, 55, 121–133, 1938.
- Fridlind, A. M., Van Diedenhoven, B., Ackerman, A. S., Avramov, A., Mrowiec, A., Morrison, H., Zuidema, P., and Shupe, M. D.: A fire-ACE/SHEBA case study of mixed-phase arctic boundary layer clouds: Entrainment rate limitations on rapid primary ice nucleation processes, *J. Atmos. Sci.*, 69, 365–389, <https://doi.org/10.1175/JAS-D-11-052.1>, 2012.
- Hashino, T. and Tripoli, G. J.: The Spectral Ice Habit Prediction System (SHIPS). Part I: Model Description and Simulation of the Vapor Deposition Process, *J. Atmos. Sci.*, 64, 2210–2237, <https://doi.org/10.1175/JAS3963.1>, 2007.
- Hashino, T. and Tripoli, G. J.: The Spectral Ice Habit Prediction System (SHIPS). Part II: Simulation of Nucleation and Depositional Growth of Polycrystals, *J. Atmos. Sci.*, 65, 3071–3094, <https://doi.org/10.1175/2008JAS2615.1>, 2008.
- Hashino, T. and Tripoli, G. J.: The Spectral Ice Habit Prediction System (SHIPS). Part III: Description of the Ice Particle Model and the Habit-Dependent Aggregation Model, *J. Atmos. Sci.*, 68, 1125–1141, <https://doi.org/10.1175/2011JAS3666.1>, 2011a.
- Hashino, T. and Tripoli, G. J.: The Spectral Ice Habit Prediction System (SHIPS). Part IV: Box Model Simulations of the Habit-

- Dependent Aggregation Process, *J. Atmos. Sci.*, 68, 1142–1161, <https://doi.org/10.1175/2011JAS3667.1>, 2011b.
- Hashino, T., De Boer, G., Okamoto, H., and Tripoli, G. J.: Relationships between immersion freezing and crystal habit for arctic mixed-phase clouds—A numerical study, *J. Atmos. Sci.*, 77, 2411–2438, <https://doi.org/10.1175/JAS-D-20-0078.1>, 2020.
- Heymsfield, A. and Westbrook, C.: A review of cloud particle types in storms and their contributions to rainfall and snowfall, *Atmos. Res.*, 97, 273–282, 2010.
- Heyn, I., Block, K., Mülmenstädt, J., Gryspeerdt, E., Kühne, P., Salzmann, M., and Quaas, J.: Assessment of simulated aerosol effective radiative forcings in the terrestrial spectrum, *Geophys. Res. Lett.*, 44, 1001–1007, <https://doi.org/10.1002/2016GL071975>, 2017.
- Hill, A.: The Kinematic Driver (KiD) model code, GitHub [code], <https://github.com/Adehill/KiD-A.git> (last access: 5 January 2023), 2023.
- Hill, A. A., Shipway, B. J., and Boutle, I. A.: How sensitive are aerosol-precipitation interactions to the warm rain representation?, *J. Adv. Model. Earth Sy.*, 7, 987–1004, <https://doi.org/10.1002/2014MS000422>, 2015.
- Hill, A. A., Lebo, Z. J., Andrejczuk, M., Arabas, S., Dziekan, P., Field, P., Gettelman, A., Hoffmann, F., Pawlowska, H., Onishi, R., and Vié, B.: Toward a Numerical Benchmark for Warm Rain Processes, *J. Atmos. Sci.*, 80, 1329–1359, <https://doi.org/10.1175/JAS-D-21-0275.1>, 2023.
- Hoffmann, F., Raasch, S., and Noh, Y.: Entrainment of aerosols and their activation in a shallow cumulus cloud studied with a coupled LCM–LES approach, *Atmos. Res.*, 156, 43–57, <https://doi.org/10.1016/j.atmosres.2014.12.008>, 2015.
- Hogan, R. J., Illingworth, A. J., Sauvageot, H., and Gaussiat, N.: Stratocumulus Liquid Water Content from Dual-Wavelength Radar, *J. Atmos. Ocean. Techn.*, 17, 379–386, 2000.
- Hogan, R. J., Westbrook, C. D., Illingworth, A. J., Wood, C. R., and Donovan, D. P.: A Variational Scheme for Retrieving Ice Cloud Properties from Combined Radar, Lidar, and Infrared Radiometer, *J. Atmos. Sci.*, 69, 634–654, 2012.
- Hogan, R. J., Honeyager, R., Tyynelä, J., and Kneifel, S.: Calculating the Millimetre-Wave Scattering Phase Function of Snowflakes Using the Self-Similar Rayleigh–Gans Approximation, *Q. J. Roy. Meteor. Soc.*, 143, 834–844, <https://doi.org/10.1002/qj.2968>, 2017.
- Hoose, C. and Möhler, O.: Heterogeneous ice nucleation on atmospheric aerosols: a review of results from laboratory experiments, *Atmos. Chem. Phys.*, 12, 9817–9854, <https://doi.org/10.5194/acp-12-9817-2012>, 2012.
- Kahn, R. A., Andrews, E., Brock, C. A., Chin, M., Feingold, G., Gettelman, A., Levy, R. C., Murphy, D. M., Nenes, A., Pierce, J. R., Popp, T., Redemann, J., Sayer, A. M., da Silva, A. M., Sogacheva, L., and Stier, P.: Reducing Aerosol Forcing Uncertainty by Combining Models With Satellite and Within-The-Atmosphere Observations: A Three-Way Street, *Rev. Geophys.*, 61, e2022RG000796, <https://doi.org/10.1029/2022RG000796>, 2023.
- Kanji, Z. A., Ladino, L. A., Wex, H., Boose, Y., Burkert-Kohn, M., Cziczo, D. J., and Krämer, M.: Overview of Ice Nucleating Particles, *Meteor. Mon.*, 58, 1.1–1.33, 2017.
- Klein, S. A., McCoy, R. B., Morrison, H., Ackerman, A. S., Avramov, A., de Boer, G., Chen, M., Cole, J. N. S., Del Genio, A. D., Falk, M., Foster, M. J., Fridlind, A., Golaz, J.-C., Hashino, T., Harrington, J. Y., Hoose, C., Khairoutdinov, M. F., Larson, V. E., Liu, X., Luo, Y., McFarquhar, G. M., Menon, S., Neggers, R. A. J., Park, S., Poellot, M. R., Schmidt, J. M., Sednev, I., Shipway, B. J., Shupe, M. D., Spangenberg, D. A., Sud, Y. C., Turner, D. D., Veron, D. E., von Salzen, K., Walker, G. K., Wang, Z., Wolf, A. B., Xie, S., Xu, K.-M., Yang, F., and Zhang, G.: Intercomparison of model simulations of mixed-phase clouds observed during the ARM Mixed-Phase Arctic Cloud Experiment. I: single-layer cloud, *Q. J. Roy. Meteor. Soc.*, 135, 979–1002, <https://doi.org/10.1002/qj.416>, 2009.
- Kneifel, S., Redl, S., Orlandi, E., Löhnert, U., Cadeddu, M. P., Turner, D. D., and Chen, M.: Snow Scattering Signals in Ground-Based Passive Microwave Radiometer Measurements, *J. Appl. Meteorol. Clim.*, 54, 1712–1729, 2015.
- Lee, J., Seifert, P., Hashino, T., Maahn, M., Fabian, S., and Knuth, O.: Numerical evidence that the impact of CCN and INP concentrations on mixed-phase clouds is observable with cloud radars, Zenodo [data set], <https://doi.org/10.5281/zenodo.8257078>, 2023.
- Lebo, Z. J. and Seinfeld, J. H.: A continuous spectral aerosol-droplet microphysics model, *Atmos. Chem. Phys.*, 11, 12297–12316, <https://doi.org/10.5194/acp-11-12297-2011>, 2011.
- Liou, K.-N. and Ou, S. S. C.: Light scattering by ice crystals: fundamentals and applications, *Prog. Energ. Combust.*, 30, 267–306, 2004.
- Maahn, M., Hoffmann, F., Shupe, M. D., de Boer, G., Matrosov, S. Y., and Luke, E. P.: Can liquid cloud microphysical processes be used for vertically pointing cloud radar calibration?, *Atmos. Meas. Tech.*, 12, 3151–3171, <https://doi.org/10.5194/amt-12-3151-2019>, 2019.
- Magono, C. and Lee, C. W.: Meteorological classification of natural snow crystals, *Journal of the Faculty of Science, Hokkaido University, Series 7 (Geophysics)*, 2, 321–335, 1966.
- Maherndl, N., Maahn, M., Tridon, F., Leinonen, J., Ori, D., and Kneifel, S.: A riming-dependent parameterization of scattering by snowflakes using the self-similar Rayleigh–Gans Approximation, *Q. J. Roy. Meteor. Soc.*, 149, 3562–3581, <https://doi.org/10.1002/qj.4573>, 2023.
- Matsui, T., Iguchi, T., Li, X., Han, M.-I., Tao, W.-K., Peters-Lidard, C., Kummerow, C., Lang, S., Meneghini, R., and Liao, L.: Evaluation of cloud microphysics schemes in simulations of a winter storm using radar and radiometer measurements, *J. Geophys. Res.-Atmos.*, 124, 639–663, 2019.
- McFarquhar, G. M. and Heymsfield, A. J.: Parameterization of Tropical Cirrus Ice Crystal Size Distributions and Implications for Radiative Transfer: Method and Preliminary Results, *J. Atmos. Sci.*, 54, 2187–2200, 1997.
- Mech, M., Maahn, M., Kneifel, S., Ori, D., Orlandi, E., Kollias, P., Schemann, V., and Crewell, S.: PAMTRA 1.0: the Passive and Active Microwave radiative TRAnSfer tool for simulating radiometer and radar measurements of the cloudy atmosphere, *Geosci. Model Dev.*, 13, 4229–4251, <https://doi.org/10.5194/gmd-13-4229-2020>, 2020.
- Miltenberger, A. K., Field, P. R., Hill, A. A., Rosenberg, P., Shipway, B. J., Wilkinson, J. M., Scovell, R., and Blyth, A. M.: Aerosol–cloud interactions in mixed-phase convective clouds –

- Part 1: Aerosol perturbations, *Atmos. Chem. Phys.*, 18, 3119–3145, <https://doi.org/10.5194/acp-18-3119-2018>, 2018.
- Mishchenko, M. I., Travis, L. D., and Lacis, A. A.: *Scattering, Absorption, and Emission of Light by Small Particles*, Cambridge University Press, ISBN 9780521782524, 1996.
- Mitchell, D. L.: Use of Mass- and Area-Dimensional Power Laws for Determining Precipitation Particle Terminal Velocities, *J. Atmos. Sci.*, 53, 1710–1723, 1996.
- Morrison, H., Curry, J. A., and Khvorostyanov, V. I.: A New Double-Moment Microphysics Parameterization for Application in Cloud and Climate Models. Part I: Description, *J. Atmos. Sci.*, 62, 1665–1677, 2005.
- Morrison, H., Thompson, G., and Tatarskii, V.: Impact of cloud microphysics on the development of trailing stratiform precipitation in a simulated squall line: Comparison of one- and two-moment schemes, *Mon. Weather Rev.*, 137, 991–1007, <https://doi.org/10.1175/2008MWR2556.1>, 2009.
- Morrison, H., Zuidema, P., Ackerman, A. S., Avramov, A., de Boer, G., Fan, J., Fridlind, A. M., Hashino, T., Harrington, J. Y., Luo, Y., Ovchinnikov, M., and Shipway, B.: Intercomparison of cloud model simulations of Arctic mixed-phase boundary layer clouds observed during SHEBA/FIRE-ACE, *J. Adv. Model. Earth Sy.*, 3, M05001, <https://doi.org/10.1029/2011MS000066>, 2011.
- Morrison, H., de Boer, G., Feingold, G., Harrington, J., Shupe, M. D., and Sulia, K.: Resilience of persistent Arctic mixed-phase clouds, *Nat. Geosci.*, 5, 11–17, <https://doi.org/10.1038/ngeo1332>, 2012.
- Mülmenstädt, J., Stevens, B., and Bony, S.: Cloud-top radiative cooling: a factor to be considered in convective self-aggregation, *J. Adv. Model. Earth Sy.*, 7, 700–714, 2015.
- Ong, C. R., Koike, M., Hashino, T., and Miura, H.: Modeling Performance of SCALE-AMPS: Simulations of Arctic Mixed-Phase Clouds Observed During SHEBA, *J. Adv. Model. Earth Sy.*, 14, 1–22, <https://doi.org/10.1029/2021ms002887>, 2022.
- Onishi, R. and Takahashi, K.: A warm-bin–cold-bulk hybrid cloud microphysical model, *J. Atmos. Sci.*, 69, 1474–1497, <https://doi.org/10.1175/JAS-D-11-0166.1>, 2012.
- Ori, D., Schemann, V., Karrer, M., and et al.: Evaluation of ice particle growth in ICON using statistics of multi-frequency Doppler cloud radar observations, *Q. J. Roy. Meteor. Soc.*, 146, 3830–3849, <https://doi.org/10.1002/qj.3875>, 2020.
- Possner, A., Ekman, A. M., and Lohmann, U.: Cloud response and feedback processes in stratiform mixed-phase clouds perturbed by ship exhaust, *Geophys. Res. Lett.*, 44, 1964–1972, <https://doi.org/10.1002/2016GL071358>, 2017.
- Radenz, M., Bühl, J., Seifert, P., Baars, H., Engelmann, R., Barja González, B., Mamouri, R.-E., Zamorano, F., and Ansmann, A.: Hemispheric contrasts in ice formation in stratiform mixed-phase clouds: disentangling the role of aerosol and dynamics with ground-based remote sensing, *Atmos. Chem. Phys.*, 21, 17969–17994, <https://doi.org/10.5194/acp-21-17969-2021>, 2021.
- Schnitt, S., Löhnert, U., and Preusker, R.: Potential of Dual-Frequency Radar and Microwave Radiometer Synergy for Water Vapor Profiling in the Cloudy Trade Wind Environment, *J. Atmos. Ocean. Tech.*, 37, 1973–1986, <https://doi.org/10.1175/JTECH-D-19-0110.1>, 2020.
- Seifert, A. and Beheng, K. D.: A two-moment cloud microphysics parameterization for mixed-phase clouds. Part 1: Model description, *Meteorol. Atmos. Physics*, 92, 45–66, <https://doi.org/10.1007/s00703-005-0112-4>, 2006.
- Seifert, A., Köhler, C., and Beheng, K. D.: Aerosol-cloud-precipitation effects over Germany as simulated by a convective-scale numerical weather prediction model, *Atmos. Chem. Phys.*, 12, 709–725, <https://doi.org/10.5194/acp-12-709-2012>, 2012.
- Seifert, P., Ansmann, A., Mattis, I., Wandinger, U., Tesche, M., Engelmann, R., Müller, D., Pérez, C., and Haustein, K.: Saharan dust and heterogeneous ice formation: Eleven years of cloud observations at a central European EARLINET site, *J. Geophys. Res.-Atmos.*, 115, D20201, <https://doi.org/10.1029/2009JD013222>, 2010.
- Shipway, B. J. and Hill, A. A.: Diagnosis of systematic differences between multiple parametrizations of warm rain microphysics using a kinematic framework, *Q. J. Roy. Meteor. Soc.*, 138, 2196–2211, <https://doi.org/10.1002/qj.1913>, 2012.
- Solomon, A., de Boer, G., Creamean, J. M., McComiskey, A., Shupe, M. D., Maahn, M., and Cox, C.: The relative impact of cloud condensation nuclei and ice nucleating particle concentrations on phase partitioning in Arctic mixed-phase stratocumulus clouds, *Atmos. Chem. Phys.*, 18, 17047–17059, <https://doi.org/10.5194/acp-18-17047-2018>, 2018.
- Tao, W. K., Chen, J. P., Li, Z., Wang, C., and Zhang, C.: Impact of aerosols on convective clouds and precipitation, *Rev. Geophys.*, 50, RG2001, <https://doi.org/10.1029/2011RG000369>, 2012.
- Thompson, G., Rasmussen, R. M., and Manning, K.: Explicit Forecasts of Winter Precipitation Using an Improved Bulk Microphysics Scheme. Part I: Description and Sensitivity Analysis, *Mon. Weather Rev.*, 132, 519–542, [https://doi.org/10.1175/1520-0493\(2004\)132<0519:EFOWPU>2.0.CO;2](https://doi.org/10.1175/1520-0493(2004)132<0519:EFOWPU>2.0.CO;2), 2004.
- Thompson, G., Field, P. R., Rasmussen, R. M., and Hall, W. D.: Explicit Forecasts of Winter Precipitation Using an Improved Bulk Microphysics Scheme. Part II: Implementation of a New Snow Parameterization, *Mon. Weather Rev.*, 136, 5095–5115, <https://doi.org/10.1175/2008MWR2387.1>, 2008.
- Twomey, S.: Pollution and the planetary albedo, *Atmos. Environ.*, 8, 1251–1256, [https://doi.org/10.1016/0004-6981\(74\)90004-3](https://doi.org/10.1016/0004-6981(74)90004-3), 1974.
- Tzivion, S., Feingold, G., and Levin, Z.: An Efficient Numerical Solution to the Stochastic Collection Equation, *J. Atmos. Sci.*, 44, 3139–3149, [https://doi.org/10.1175/1520-0469\(1987\)044<3139:AENSTT>2.0.CO;2](https://doi.org/10.1175/1520-0469(1987)044<3139:AENSTT>2.0.CO;2), 1987.
- Tzivion, S., Feingold, G., and Levin, Z.: The evolution of raindrop spectra. Part II: Collisional collection/breakup and evaporation in a rainshaft, *J. Atmos. Sci.*, 46, 3312–3328, [https://doi.org/10.1175/1520-0469\(1989\)046<3312:TEORSP>2.0.CO;2](https://doi.org/10.1175/1520-0469(1989)046<3312:TEORSP>2.0.CO;2), 1989.
- Ulaby, F. T., Moore, R. K., and Fung, A. K.: *Microwave Remote Sensing: Active and Passive*, in: Artech House microwave library, Artech House, 456 pp., ISBN 9780890061909, 1981.
- Um, J. and McFarquhar, G. M.: An update on the ice particle scattering database for radiative transfer studies, *J. Quant. Spectrosc. Ra.*, 112, 650–652, 2011.
- Vázquez-Martín, S., Kuhn, T., and Eliasson, S.: Shape dependence of snow crystal fall speed, *Atmos. Chem. Phys.*, 21, 7545–7565, <https://doi.org/10.5194/acp-21-7545-2021>, 2021.
- Vié, B., Pinty, J.-P., Berthet, S., and Leriche, M.: LIMA (v1.0): A quasi two-moment microphysical scheme driven by a multimodal population of cloud condensation and ice freezing nuclei,

- Geosci. Model Dev., 9, 567–586, <https://doi.org/10.5194/gmd-9-567-2016>, 2016.
- von Lerber, A., Mech, M., Rinke, A., Zhang, D., Lauer, M., Radovan, A., Gorodetskaya, I., and Crewell, S.: Evaluating seasonal and regional distribution of snowfall in regional climate model simulations in the Arctic, *Atmos. Chem. Phys.*, 22, 7287–7317, <https://doi.org/10.5194/acp-22-7287-2022>, 2022.
- Westbrook, C. D. and Illingworth, A. J.: The fall speeds of sub-100 μm ice crystals, *Q. J. Roy. Meteor. Soc.*, 137, 1266–1281, 2011.
- Zängl, G., Reinert, D., Rípodas, P., and Baldauf, M.: The ICON (ICOsahedral Non-hydrostatic) modelling framework of DWD and MPI-M: Description of the non-hydrostatic dynamical core, *Q. J. Roy. Meteor. Soc.*, 141, 563–579, <https://doi.org/10.1002/qj.2378>, 2015.
- Zhang, D., Wang, Z., Kollias, P., Vogelmann, A. M., Yang, K., and Luo, T.: Ice particle production in mid-level stratiform mixed-phase clouds observed with collocated A-Train measurements, *Atmos. Chem. Phys.*, 18, 4317–4327, <https://doi.org/10.5194/acp-18-4317-2018>, 2018.